COLLAPSE OF OPTICAL VORTICES AND SEQUENTIAL FILAMENTATION

A Dissertation

Presented to the Faculty of the Graduate School

of Cornell University

in Partial Fulfillment of the Requirements for the Degree of

Doctor of Philosophy

by

Luat Thanh Vuong

January 2009

COLLAPSE OF OPTICAL VORTICES AND SEQUENTIAL FILAMENTATION

Luat Thanh Vuong, Ph.D.

Cornell University 2009

This thesis presents investigations of nonlinear light propagation dynamics in isotropic self-focusing materials. The first half of this thesis is devoted to studying the transverse spatial dynamics of optical vortices, donut-shaped beams with helical phase fronts. The second half of this thesis describes the spatiotemporal dynamics of sequential plasma filaments that are formed by high-peak power laser pulses. The objective of these studies is to identify novel behavior, to predict nonlinear trends, and to achieve a new understanding of the physical processes that govern the dynamics of high-power beams and pulses.

BIOGRAPHICAL SKETCH

My mother is ethnic Chinese, born in Hong Kong, and my father is ethnic Vietnamese, born in Cambodia. I have a sister, Luan, and a brother, Ben, 2 and 6 years my junior, respectively and we lived in Canada until I was 9, at which point we moved to Northern Virginia. Luan beat me in a tennis match when was 12, and I haven't picked up a tennis racket ever since. Although Luan and I studied piano, violin, viola, and cello, Ben instead chose to take up the drums, and at age 17, because of him, I remember practicing double stroke rolls secretly when home alone.

I attended U.C. Berkeley in 1994, having never tried sushi and believing that a futon was a New Stone Age tool. I volunteered, I lived in residential cooperatives, and many core values were shaped by a fabulous diversity of opinions in the people I met, students and professionals (and even some nonprofessionals). After graduating, I worked at Dicon Fiberoptics, a Taiwanese manufacturing company, where among many things I learned how to gossip in Chinese. I also worked at Onix Microsystems, a startup involving U.C. Berkeley Professor Kam Lau, who supported my initial bid for graduate school.

My next endeavor will be to improve third-generation solar cells, and my efforts will begin at the ICFO-Institute of Photonic Sciences in Barcelona, Spain this autumn.

“There is a joke that your hammer will always find nails to hit.

I find that perfectly acceptable.”

-Benoit Mandelbrot

ACKNOWLEDGEMENTS

Professor Alexander Gaeta has been my essential dispenser-of-wisdom and academic guardian, but he has also inspired me with his leadership, kindness, and commitment to teaching. I want to thank him, in particular, for generously agreeing to my Fulbright research venture in the last year of my Ph.D.

I am grateful to Sheryl Woodward and the AT&T Labs Fellowship Program, who have provided funding and mentoring for six years. I also appreciate the University of Colorado at Boulder optics faculty and the cycling team for providing valuable training and seeding my interest in nonlinear dynamics. My research improved considerably due to contributions from collaborators E.R. Eliel, G. Fibich, C.P. Hauri, R.B.Lopez-Martens and G.'t Hooft. I thank them and committee members C. Xu and R.H. Rand for guidance and support.

Oak : tree :: the Gaeta research group : extended family. To KDM, DH, DGO, SG, TDG, MAF, YO, IHA, AB, CJH, DB, SS, VV, then JS, AAI, PL, BGS, AS, and RS, even MES and UGS– it's extraordinary how each one of us leads in his own unique way. Within this gradschool enclave, I have learned and benefit tremendously from you.

I thank MLH, VEH, and TR for sharing cold rides and sultry scenery, MB and JLL for being loverly, BT and HT for culinary treats and weekend retreats, SC and NC for Southside living, TEJ and ZG for just being sassysmart doers, CCC for nats, all who came to my XXX on the Arts quad, GAC for providing home when I was homeless. And SNL for always criticizing and always challenging me, while believing in me.

Lastly... I am simply indebted to my family for their unyielding care. With parents so unselfish and siblings so genuinely intelligent and thoughtful, I can never forget that I am the product of favorable circumstances and inherited luck.

TABLE OF CONTENTS

LIST OF FIGURES

CHAPTER 1

INTRODUCTION

A system is nonlinear when the constituent behavior changes due to interactions with itself. Because of the interactions, certain dynamics can be amplified over others and produce a system attractor, where a range of initial conditions evolve into an equivalent state. This broadly classifies self-organization and pattern formation dynamics in nonlinear systems, which are investigated in a wide range of fields including optics, fluids, plasma physics, and material science [19]. Nonlinear systems can also exhibit bifurcations, where small changes in the initial conditions lead to different system attractors, also known as a phase transition. Lines of bifurcation characterize a nonlinear system and are studied in many disciplines [110] because they provide insight into the ways in which dynamics can be controlled. In physics, steep switching mechanisms can be used to measure environmental parameters and moreover, have communications applications.

The optical nonlinearities of isotropic materials studied in this thesis are due to electronic responses of bound and liberated electrons; other physical processes, for example the motion of molecules, occur at timescales longer than the laser pulse duration and therefore have insignificant involvement with the laser pulse. Light can be confined over distances several orders of magnitude greater than its confocal parameter by the combined effects of self-focusing and light-induced gas ionization [11]. The formation of light filaments has been shown to be robust to perturbations [18], and the onset of filamentation and multiple filamentation spatial patterns are controllable by several means [28, 39, 45, 48, 53, 70]. Experiments involving high-power filaments contribute

to our understanding of fundamental physical processes and offer an array of potential applications [42, 57, 98, 111].

In section 1.1 the intensity-dependent refractive index is described and the Nonlinear Schrödinger evolution equation for modeling the self-focusing of electric fields in the paraxial limit is derived. In section 1.1.3 we demonstrate the evolution of an electric field filament to the two-dimensional Townes profile attractor and describe the pattern formation that arises from a modulational instability. In section 1.2 we derive the nonlinear envelope equation that accounts for gas ionization [section 1.2.1] and high-order temporal effects in the propagation dynamics [section 1.2.2]. This approach rederives the identical evolution equation used in [76] using a frequency-domain approach, and but contains a different coefficient involving the plasma absorption. The frequency-domain analysis is helpful for integrating broadband dispersion corrections, which are discussed in section 3.3.

In chapter 2, the angular momentum of light is introduced. This chapter combines the investigations of collapse and multiple-filamentation dynamics for homogeneously-polarized optical vortices and inhomogeneously-polarized beams [105, 106, 107]. In our investigations of self-focusing optical vortices in Kerr media, we show how vortices evolve to a distinct self-similar profile, which becomes unstable to azimuthal perturbations. We predict the dynamics of these instabilities and verify our claims numerically and experimentally. With copropagating orthogonal-circularly polarized beams, we observe that optical vortices with different topological charge spatially separate during multiple-filamentation and we explain the origin of this effect. New dynamics accompany this spatial separation of azimuthal instabilities, and we experimentally

measure the OAM switching and polarization rotation that occurs via nonequilibrium phase transitions.

In chapter 3 we describe the spectral reshaping that occurs as a result of the sequential formation of two on-axis plasma filaments or sequential filamentation. We provide a theoretical description of the spatio-temporal dynamics of sequential filamentation in noble gases that can lead to pulse compression down to nearly single-cycle pulses. We show that the strong pulse compression occurs as a result of serially-generated on-axis filaments and spectral filtering of an extensive blue-shifted compressible spectra. We show that the dynamics of this sequential filamentation can be readily tuned by varying the gas pressure and can be scaled to various pulse energies. We provide a theoretical description of optimal pulse compression via filamentation and we propose that the alternating dynamics between beam focusing and defocusing and the production of visible sequential plasma filaments is the primary mechanism that leads to the extensive blue-shifted spectrum which enables pulse compression.

In the conclusion, potential directions for further investigating filamentation are outlined.

1.1 Derivation of Nonlinear Schrödinger Equation

The challenge of modeling the propagation of electromagnetic fields generally lies in simplifying Maxwell's equations. In this thesis, we consider nonmagnetic isotropic materials where Maxwell's equations are represented as

$$\nabla \cdot \tilde{\mathbf{E}} = \frac{1}{n_0^2}\Big[4\pi\rho_{free} - 4\pi\nabla \cdot \tilde{\mathbf{P}}_{NL}\Big], \tag{1.1}$$

$$\nabla \times \tilde{\mathbf{E}} = -\frac{1}{c}\frac{\partial \tilde{\mathbf{H}}}{\partial t}, \tag{1.2}$$

$$\nabla \cdot \tilde{\mathbf{H}} = 0, \tag{1.3}$$

$$\nabla \times \tilde{\mathbf{H}} = \frac{1}{c}\frac{\partial}{\partial t}\left[n_0^2 \tilde{\mathbf{E}} + 4\pi \tilde{\mathbf{P}}_{NL}\right] + 4\pi \tilde{\mathbf{J}}, \tag{1.4}$$

where $\tilde{\mathbf{E}}$ and $\tilde{\mathbf{H}}$ are the electric and the magnetic fields, $\tilde{\mathbf{J}}$ is the electron current density, ρ is the free electron density, n_0 is the linear refractive index, c is the speed of light and $\tilde{\mathbf{P}}_{NL}$ is the nonlinear contribution of the material polarization due to bound charges. When we take the curl of both sides of Eq. 1.2, substitute Eq. 1.4, and apply the vector identity $\nabla \times (\nabla \times \tilde{\mathbf{E}}) = \nabla(\nabla \cdot \tilde{\mathbf{E}}) - \nabla^2 \tilde{\mathbf{E}}$, the result

$$\nabla(\nabla \cdot \tilde{\mathbf{E}}) - \nabla^2 \tilde{\mathbf{E}} = -\frac{1}{c}\frac{\partial}{\partial t}\left[\frac{1}{c}\frac{\partial (n_0^2 \tilde{\mathbf{E}} + 4\pi \tilde{\mathbf{P}}_{NL})}{\partial t} + 4\pi \tilde{\mathbf{J}}\right], \tag{1.5}$$

is a wave equation with additional terms. In this thesis, we assume that the material in which the electromagnetic field is propagating has no net charge or $\rho_{free} = 0$, and the first term on the right hand side if Eq. 1.1 vanishes. Substituting and distributing terms in Eq. 1.5, Maxwell's equations for the electric fields in an isotropic nonlinear material are written

$$\frac{n_0^2}{c^2}\frac{\partial^2}{\partial t^2}\tilde{\mathbf{E}} - \nabla^2 \tilde{\mathbf{E}} = -\frac{4\pi}{c^2}\frac{\partial^2}{\partial t^2}\tilde{\mathbf{P}}_{NL} + \frac{4\pi}{n_0^2}\nabla(\nabla \cdot \tilde{\mathbf{P}}_{NL}) - \frac{4\pi}{c}\frac{\partial}{\partial t}\tilde{\mathbf{J}}. \tag{1.6}$$

We consider the dynamics associated with the third-order nonlinear optical interactions and a nonlinear polarization $\tilde{\mathbf{P}}_{NL}$ that result in pure self-focusing. Second-order effects, by symmetry, typically do not occur in isotropic media, although there are exceptions, namely the case where a third-order nonlinear polarization produces sufficient asymmetry to generate second-harmonic [75]. These and higher-order harmonics are neglected because even during extended propagation, the additional frequency components do not contribute appreciably to the nonlinear propagation dynamics [62]. Self-focusing occurs due to an intensity dependent refractive index that is defined

$$n = n_0 + n_2 I \tag{1.7}$$

where

$$I = \frac{n_0}{2\pi}|\tilde{\mathbf{E}}|^2 \tag{1.8}$$

Without a formal derivation using the fourth-rank tensor nonlinear susceptibility, the nonresonant electronic response is represented,

$$\tilde{\mathbf{P}}_{NL} = \frac{n_0^2 n_2 c}{2\pi^2}\Big[(\tilde{\mathbf{E}}\cdot\tilde{\mathbf{E}}^*)\tilde{\mathbf{E}} + \frac{1}{2}(\tilde{\mathbf{E}}\cdot\tilde{\mathbf{E}})\tilde{\mathbf{E}}^*\Big], \tag{1.9}$$

which assumes Kleinman symmetry, or that the average position of the electrons is unchanged due to presence of the electric field. Therefore, we also neglect light-induced effects on the electron behavior due to radiation pressure or ponderomotive forces. For the remaining subsections in section 1.1, we assume that there are no charged carriers, or $\tilde{\mathbf{J}} = 0$, however, in section 1.2, $\tilde{\mathbf{J}}$ is reintroduced to derive the nonlinear envelope equation. We also return to this vectorial treatment of Maxwell's equations [Eq. 1.6] in order to discuss higher-order polarization effects in the generation of plasma for future experiments [section 3.3].

1.1.1 Vectorial Effects and Assumptions Related to $\tilde{\mathbf{P}}_{\mathbf{NL}}$

We simplify the tensor form of Eq. 1.6 and Eq. 1.9 into scalar contributions of an electric field using two similar approximations that both assume electric fields with light rays are parallel to the direction of propagation. The first assumption in the analysis of Eq. 1.6 is that the second term on the right-hand side is zero,

$$\nabla(\nabla\cdot\tilde{\mathbf{P}}_{NL}) \approx 0. \tag{1.10}$$

Since the nonlinear polarization $\tilde{\mathbf{P}}_{NL}$ grows and vanishes depending on the evolving spatial beam profile of $\tilde{\mathbf{E}}$, its divergence $\nabla\cdot\tilde{\mathbf{P}}_{NL} \neq 0$. In order for Equa-

tion 1.10 to remain valid, the transverse spatial beam profile must not change rapidly, either in the transverse direction or during propagation.

The second approximation involves the calculation of the nonlinear polarization [Eq. 1.9], where we also assume that longitudinal field components are small, or

$$\tilde{\mathbf{E}} = \tilde{A}(\mathbf{x}, t)\hat{\mathbf{e}} + \tilde{\Delta}(\mathbf{x}, t)\hat{\mathbf{k}} \tag{1.11}$$

$$\approx \tilde{A}(\mathbf{x}, t)\hat{\mathbf{e}}, \tag{1.12}$$

where $\hat{\mathbf{e}}$ is the polarization vector that lies in the transverse or $x - y$ plane and $\hat{\mathbf{k}}$ points in the z-direction. This is equivalent to the claim that the transverse spatial beam profile does not change appreciably; the longitudinal field component generally scales in proportion with the transverse gradient and inversely with the wavenumber, which is large at optical wavelengths.

Neglecting the longitudinal field component, we now find that the nonlinear polarization $\tilde{\mathbf{P}}_{NL}$ depends on the polarization of light. If $\tilde{\mathbf{E}}$ is linearly-polarized along the $\hat{\mathbf{i}}$-direction or along the x-axis, then since

$$\hat{\mathbf{i}}^* = \hat{\mathbf{i}}, \tag{1.13}$$

$$\hat{\mathbf{i}} \cdot \hat{\mathbf{i}} = 1, \tag{1.14}$$

$$\tilde{\mathbf{P}}_{NL}^{LP} = \frac{3n_0^2 n_2 c}{4\pi^2}|\tilde{A}|^2\tilde{A}\hat{\mathbf{i}}, \tag{1.15}$$

Eq. 1.6 can be simplified,

$$\frac{n_0^2}{c^2}\frac{\partial^2}{\partial t^2}\tilde{A} - \nabla^2\tilde{A} = -\frac{n_0^2 n_2 c}{\pi}\frac{12}{c^2}\frac{\partial^2}{\partial t^2}|\tilde{A}|^2\tilde{A}, \tag{1.16}$$

which is also known as the nonlinear Helmholtz equation. Alternatively, if we consider a circularly-polarized beam $\hat{\mathbf{e}} = \hat{\sigma}_{\pm}$ denoting a right (-) or left(+)

circularly-polarized field, then

$$\hat{\sigma}_{\pm} = (\hat{\mathbf{i}} \pm i\hat{\mathbf{j}})/\sqrt{2} \tag{1.17}$$

$$\hat{\sigma}_{\pm}^{*} = \hat{\sigma}_{\mp}, \tag{1.18}$$

$$\hat{\sigma}_{\pm} \cdot \hat{\sigma}_{\pm} = 0, \tag{1.19}$$

$$\hat{\sigma}_{\pm} \cdot \hat{\sigma}_{\mp} = 1, \tag{1.20}$$

and consequently,

$$\tilde{\mathbf{P}}_{NL}^{CP} = \frac{n_0^2 n_2 c}{2\pi^2} |\tilde{A}|^2 \tilde{A} \hat{\sigma}_{\pm}. \tag{1.21}$$

Since the magnitude of the nonlinear polarization scales according to the electric field polarization,

$$|\tilde{\mathbf{P}}_{NL}^{CP}| = \frac{2}{3} |\tilde{\mathbf{P}}_{NL}^{LP}|, \tag{1.22}$$

we observe similar dynamics circular-polarized and linearly-polarized input beams at different field intensities.

To evaluate the nonlinear evolution of inhomogeneously-polarized fields, we treat orthogonal-circularly-polarized fields separately in coupled scalar wave equations. A spatially-varying polarization of an electric field

$$\tilde{\mathbf{E}} = \tilde{A}_{+}(\mathbf{x}, t)\hat{\sigma}_{+} + \tilde{A}_{-}(\mathbf{x}, t)\hat{\sigma}_{-} \tag{1.23}$$

is described by the coupled scalar equations involving $\tilde{A}_{+}$ and $\tilde{A}_{-}$

$$\frac{n_0^2}{c^2}\frac{\partial^2}{\partial t^2}\tilde{A}_{\pm} - \nabla^2 \tilde{A}_{\pm} = -\frac{n_0^2 n_2 c}{\pi}\frac{12}{c^2}\frac{\partial^2}{\partial t^2}(|\tilde{A}_{\pm}|^2 + 2|\tilde{A}_{\mp}|)\tilde{A}_{\pm}. \tag{1.24}$$

It is not difficult to show that when considering a linearly-polarized field represented in the circular-polarization basis, or $|\tilde{A}_{\pm}| = 1/\sqrt{2}$ that Eq. 1.24 becomes Eq. 1.16.

1.1.2 The Slowly-varying Envelope Approximation

The electric field and nonlinear polarization are represented by their carrier frequency envelope

$$\tilde{\mathbf{E}} = Ae^{-i(\omega t - kz)}\hat{\mathbf{e}}, \tag{1.25}$$

$$\tilde{\mathbf{P}} = Pe^{-i(\omega t - kz)}\hat{\mathbf{e}}. \tag{1.26}$$

In order to focus on the transverse nonlinear dynamics, we assume that A and P do not change with time and $\partial_t = -i\omega$. Transferring into a reference frame that travels at the speed with this continuous wave field, or $\tau = t - \frac{n_0 z}{c}$, and $\partial_z = \partial_\zeta - n_0/c\partial_\tau$.

$$\frac{-\omega^2 n_0^2}{c^2}A - (\nabla_\perp^2 + \frac{\partial^2}{\partial\zeta^2} - \frac{n_0}{c}\frac{\partial^2}{\partial\zeta\partial\tau} + \frac{n_0^2}{c^2}\frac{\partial^2}{\partial\tau^2})A = \frac{n_0^2 n_2 c}{\pi}\frac{12\omega^2}{c^2}(|A_\pm|^2 + 2|A_\mp|)A_\pm. \tag{1.27}$$

The first and last terms on the left-hand side cancel when we operate $\partial_\tau = -i\omega$, since $k = n_0\omega/c$. We invoke the slowly-varying approximations that

$$\frac{\partial A}{\partial\zeta} << kA \tag{1.28}$$

to arrive at the Nonlinear Schrödinger Equation

$$\frac{\partial}{\partial\zeta}A = \frac{i}{k}\nabla_\perp^2 A + \frac{in_0 n_2}{\pi}\frac{12\omega}{c^2}\Big(|A_\pm|^2 + 2|A_\mp|\Big)A_\pm. \tag{1.29}$$

In chapter 2 of this thesis, we normalize this equation and its variables,

$$\frac{\partial}{\partial\zeta}\psi_\pm = i\nabla_\perp^2\psi_\pm + i\beta\Big[|\psi_\pm|^2 + 2|\psi_\mp|^2\Big]\psi_\pm, \tag{1.30}$$

where $\psi_\pm$ is the scaled transverse profile associated with spin-polarized electric fields, $\sqrt{C}\psi_\pm(\rho,\theta,\zeta) = A_\pm(r,\theta,z)$ and C is a normalization constant such that $\int[|\psi_+|^2 + |\psi_-|^2]\rho\, d\rho\, d\theta = 1$. The propagation variable is $\zeta = z/kw_0^2$, and the normalized radius is $\rho = r/w_0$, where $k = 2\pi n_0/\lambda$, and w_0 is the mode field radius

of the initial beam. The coefficient $\beta = \alpha P\pi/3P_{cr}$ where the power $P = n_0 cC/2\pi$ and where α is a shape-dependent parameter for which the critical power is defined [35]. The second and third terms on the right represent self-action effects or self-focusing and cross-phase modulation, respectively. Initial beam profiles are width-normalized so that the mode field radius $\int \rho^2[|\psi_+|^2 + |\psi_-|^2]\rho\, d\rho\, d\theta = 1$, which is essential for comparing the angular momentum dynamics in chapter 2.

1.1.3 Self-similar Collapse and Modulational Instability

A gaussian beam with power greater than the critical power for self-focusing P_{cr} will be trapped in its self-induced nonlinear potential, wherein each light filament holds a precise quanta of power and, in the absence of temporal effects or higher-order terms, will undergo collapse [60]. The self-similar evolution toward collapse is illustrated in Fig. 1.1(a) where the peak field intensities asymptotically approach infinity, while the beam radius scales inversely [77]. Regardless of the initial shape, the collapsing portion of the beam converges towards a distinct profile, while the remaining portion diffracts. This self-similar profile is an attractor also known as a Townes profile [14], and can be calculated numerically assuming that the electric field has the form ψ_{norm}

$$\psi(\zeta, \rho, \theta)_{norm} = L(\zeta)\psi\left(\zeta, \frac{\rho}{L(\zeta)}, \theta\right), \tag{1.31}$$

where $L(\zeta) = \frac{1}{max|\psi|}$. The unique solution to the Nonlinear Schrödinger Equation after a lens transformation can be solved given an asymptotic rate for $L(\zeta)$. In Fig. 1.1(b) we display an experimental image of an irregularly-shaped background diffracting with a single round filament at its center with the Townes

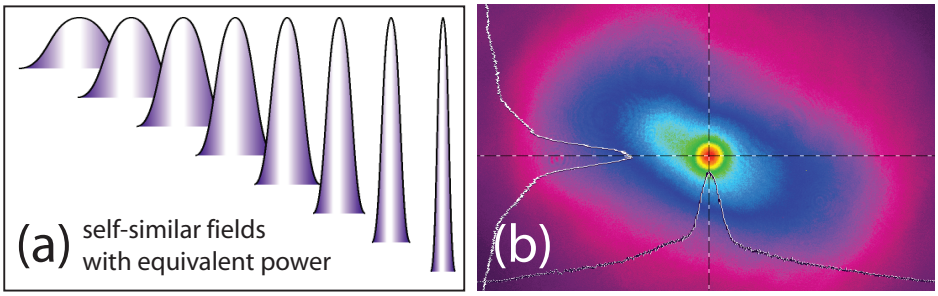

Figure 1.1: (a) Self-similar profiles with equivalent power. (b) Experimental image of a round Townes profile in the cross-section of a filament, with an irregularly-shaped background diffracting describing the results of K.D.Moll *et al.*, Phys. Rev. Lett. (2003).

profile. In section 2.1, we demonstrate a new self-similar profile that manifests in the collapse of optical vortices.

When an electric field carries more power than the critical power for self-focusing, we can observe the formation of multiple-filaments in the spatial beam profile. Spatial features of an optical beam in a Kerr medium can arise from modulational instability (MI) [6], which can lead to multiple-filamentation (MF). These MF patterns can be dramatically manipulated with beam shape [4, 28], and the noise that seeds the MI does little to change the overall MF patterns [34]. In Fig. 1.2 we show the power-dependent filamentation patterns induced by input beam ellipticity [46]. At low powers, the elliptically-shaped beams form a single filament on axis. The periodic bands of filaments that arise in the vertical and horizontal dimensions are associated with modulational instabilities in the bands. In section 2.1 we analyze the modulational instabilities associated with optical vortices and in section 2.3 we study deterministic vortex multiple-filamentation patterns that are induced by elongating the spatial beam profile.

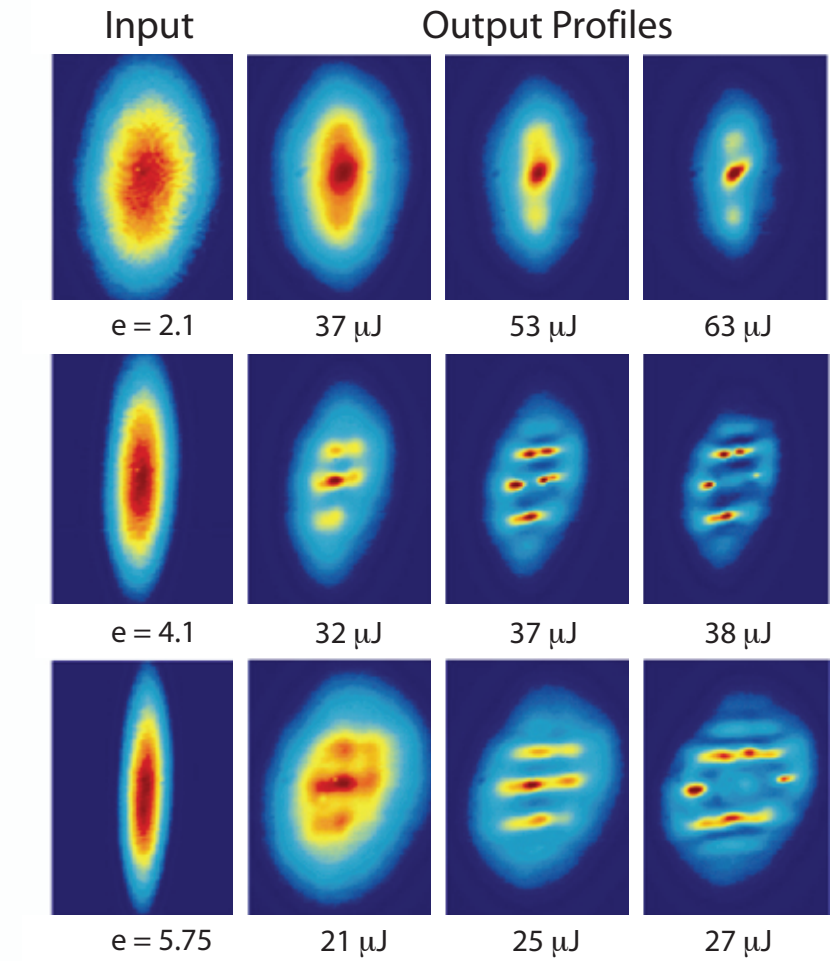

Figure 1.2: Power-dependent filamentation patterns influenced by input beam ellipticity from T.D. Grow *et al.,* Opt. Express (2005).

1.2 Nonlinear Envelope Equation

The Nonlinear Envelope Equation derived in this section considers a frequency-dependent linear refractive index $n_0(\omega)$ and the ionization of gas molecules by high-power pulses. Here we begin using Eq. 1.6 and make the paraxial assumptions described by Eqs. 1.10 and 1.11,

$$\frac{n_0^2}{c^2}\frac{\partial^2}{\partial t^2}\tilde{\mathbf{E}} - \nabla^2\tilde{\mathbf{E}} = -\frac{4\pi}{c^2}\frac{\partial^2}{\partial t^2}\tilde{\mathbf{P}}_{NL} - \frac{4\pi}{c}\frac{\partial}{\partial t}\tilde{\mathbf{J}}. \tag{1.32}$$

Since the wavenumber is dependent on frequency $k(\omega) = n_0(\omega)\omega/c$, we represent its expansion about the electric field carrier frequency,

$$\begin{aligned} \frac{n_0(\omega)}{c}(\omega) &= k(\omega) && (1.33) \\ &= k_0 + k_1(\omega - \omega_0) + \frac{1}{2}k_2(\omega - \omega_0)^2 + \mathbf{O}(\omega - \omega_0)^3, && (1.34) \end{aligned}$$

and truncate the expansion. We also make the approximation that $k_1/k_0 = 1/\omega_0$,

$$\frac{n_0\omega_0}{c}(\omega) \approx k_0\frac{\omega}{\omega_0} + \frac{1}{2}k_2(\omega - \omega_0)^2, \tag{1.35}$$

which is a valid approximation when the group and phase velocity are equal at the carrier frequency $\omega = \omega_0$. In simplifying the time derivatives of the electric field,

$$FT\left[\left(\frac{n_0(\omega)}{c}\right)^2\frac{\partial^2}{\partial t^2}\tilde{\mathbf{E}}\right] = -k(\omega)^2\tilde{\mathbf{E}}, \tag{1.36}$$

we assume that $k_2(\omega - \omega_0)^2 << k_0$ and

$$k(\omega)^2 \approx k_0^2\left(\frac{\omega}{\omega_0}\right)^2 + k_0\frac{\omega}{\omega_0}k_2(\omega - \omega_0)^2. \tag{1.37}$$

We also represent the electric field vector using its scalar envelope $A(r, \omega - \omega_0, z)$ with carrier frequency centered about ω_0,

$$\begin{aligned} \tilde{\mathbf{E}}(r, t, z) &= \int \tilde{\mathbf{E}}(r, \omega, z)e^{-i\omega t}d\omega && (1.38) \\ \tilde{\mathbf{E}}(r, \omega, z) &= A(r, \omega - \omega_0, z)e^{ik(\omega)z}\hat{\mathbf{e}} && (1.39) \\ &\approx A(r, \omega - \omega_0, z)e^{ik_0 z}\hat{\mathbf{e}}. && (1.40) \end{aligned}$$

Here, the approximation made between lines 1.39 and 1.40 allow us to consider that the electric field envelope in the time domain is the fourier transform of the frequency-domain envelope, or

$$FT[A(\omega - \omega_0)] = A(t)e^{i\omega_0 t}, \tag{1.41}$$

which is only a valid approximation for small-bandwidth pulses.

The transverse laplacian in Eq. 1.32 becomes

$$\nabla^2\tilde{\mathbf{E}} = \left[\nabla_\perp^2 + \frac{\partial^2}{\partial z^2} - 2ik_0\frac{\partial}{\partial z} - k_0^2\right]Ae^{ik_0 z}\hat{\mathbf{e}}. \tag{1.42}$$

We change variables to move in a reference frame that travels at the speed with the pulse, or $\tau = t - n_0(\omega_0)z/c$, and $\partial_z = \partial_\zeta - k_1\partial_\tau$, which results in ζ-derivatives,

$$\frac{\partial}{\partial z}A = \frac{\partial}{\partial \zeta}A - \frac{k_0}{\omega_0}\frac{\partial}{\partial \tau}A, \tag{1.43}$$

$$\frac{\partial^2}{\partial z^2}A = \frac{\partial^2}{\partial \zeta^2}A - 2\frac{k_0}{\omega_0}\frac{\partial}{\partial \tau}\frac{\partial}{\partial \zeta}A + \left(\frac{k_0}{\omega_0}\right)^2\frac{\partial^2}{\partial \tau^2}A. \tag{1.44}$$

Let $\Omega = \omega - \omega_0$ be the Fourier transform pair variable with τ. If we make the slowly-varying envelope approximation, the left hand side of Eq. 1.32 becomes

$$\begin{aligned} -\nabla^2\tilde{\mathbf{E}} - k(\Omega)^2\tilde{\mathbf{E}} = {} & \left\{ -\nabla_\perp^2 + \left[2\tfrac{ik_0\Omega}{\omega_0}\tfrac{\partial}{\partial\zeta} - \left(\tfrac{k_0}{\omega_0}\right)^2\Omega^2\right] + 2ik_0\left[\tfrac{\partial}{\partial\zeta} + \tfrac{k_0}{\omega_0}i\Omega\right]\right. \\ & \left. -k_0^2 - k_0^2\left(\tfrac{\Omega+\omega_0}{\omega_0}\right)^2 - k_0\tfrac{\Omega+\omega_0}{\omega_0}k_2\Omega^2\right\}Ae^{ik_0z}\hat{\mathbf{e}} \qquad (1.45) \\ = {} & -\left\{\nabla_\perp^2 - k_0\tfrac{\Omega+\omega_0}{\omega_0}\left[2i\tfrac{\partial}{\partial\zeta} - k_2\Omega^2\right]\right\}Ae^{ik_0z}\hat{\mathbf{e}} \qquad (1.46) \end{aligned}$$

If we assume that the nonlinear polarization vector and current density have the same direction and carrier as the electric field,

$$\tilde{\mathbf{P}}_{NL} = p(\Omega)e^{-i[(\Omega+\omega_0)t-k_0z]}\hat{\mathbf{e}} \tag{1.47}$$

$$\tilde{\mathbf{J}} = j(\Omega)e^{-i[(\Omega+\omega_0)t-k_0z]}\hat{\mathbf{e}}. \tag{1.48}$$

The scalar nonlinear envelope equation becomes,

$$-\left\{\nabla_\perp^2 + k_0\frac{\Omega+\omega_0}{\omega_0}\left[2i\frac{\partial}{\partial\zeta} - k_2\Omega^2\right]\right\}A = \frac{4\pi}{c^2}(\Omega+\omega_0)^2p + \frac{4\pi i}{c}(\Omega+\omega_0)j \tag{1.49}$$

The next 2 sections will simplify the right-hand side of Eq. 1.49 and calculate the nonlinear polarization and current density envelopes, p and j.

1.2.1 The Nonlinear Polarization Envelope p

The intense electric fields generate charged carriers due to multi-photon ionization,

$$\frac{\partial \rho}{\partial \tau} = \frac{\beta^{(m)} I_0^m}{m\hbar\omega_0}, \tag{1.50}$$

where ρ is the density of charged carriers, $\beta^{(m)}$ is the m-photon ionization coefficient, m is the number of photons needed to liberate the electron from the valence band, and I_0 is the intensity of the electric field.

To account for the energy transferred in the electric field for excitation and ionization of the propagation material, we must consider the real and imaginary parts of the nonlinear polarization. To calculate the nonlinear polarization, we assume the input electric field is linearly-polarized [Eq. 1.15] and that the nonlinear polarization $\tilde{\mathbf{P}}_{NL}$ has the same vector direction as the electric field. We define the real and imaginary envelopes of the nonlinear polarization

$$p = (p_n + i p_\alpha). \tag{1.51}$$

Here we follow a method similar to Geissler [44] where the nonlinear polarization is derived from the classical trajectory $\tilde{\mathbf{x}}(t)$ of the bound electron,

$$\frac{\partial}{\partial t}\tilde{\mathbf{P}} = \tilde{\mathbf{J}}_b = e\frac{\partial \rho}{\partial t}\tilde{\mathbf{x}} + e\rho\frac{\partial \tilde{\mathbf{x}}}{\partial t}, \tag{1.52}$$

where $\rho(t)$ is the electron density. Taking a second derivative with respect to t:

$$\frac{\partial^2}{\partial t^2}\tilde{\mathbf{P}} = e\frac{\partial^2 \rho}{\partial t^2}\tilde{\mathbf{x}} + e\rho\frac{\partial^2 \tilde{\mathbf{x}}}{\partial t^2} + 2e\frac{\partial \tilde{\mathbf{x}}}{\partial t}\frac{\partial \rho}{\partial t}, \tag{1.53}$$

A common approximation is assumes that at the instant at which a bound electron is ionized, its velocity is negligible,

$$\frac{\partial \tilde{\mathbf{x}}}{\partial t} \sim 0, \tag{1.54}$$

and the two remaining terms of Eq. 1.53 are associated with absorption and refraction, respectively,

$$\frac{\partial^2 \rho}{\partial t^2}\tilde{\mathbf{x}} = \frac{\partial^2 \tilde{\mathbf{P}}_\alpha}{\partial t^2}, \tag{1.55}$$

$$e\rho\frac{\partial^2 \tilde{\mathbf{x}}}{\partial t^2} = \frac{\partial^2 \tilde{\mathbf{P}}_n}{\partial t^2}, \tag{1.56}$$

the second equation of which is equivalently analyzed in [10]. The nonlinear polarization is, as before, an intensity-dependent change in the refractive index:

$$\tilde{p}_n(\Omega) = 3\widetilde{\overline{\chi}}^{(3)}|A(\Omega)|^2 A(\Omega) \tag{1.57}$$

To find $\tilde{p}_\alpha(\Omega)$, Geissler assumes that the electron is "born" via multiphoton ionization on the outer side of the Coulomb barrier at a distance of

$$\tilde{\mathbf{x}}(t) = \frac{I_0}{e\tilde{\mathbf{E}}^*(t)} = \frac{I_p}{eI(t)}\tilde{\mathbf{E}}(t) \tag{1.58}$$

where I_0 is the ionization potential, $I_0 \sim n\hbar\omega_0$, and $I(t) = |\tilde{\mathbf{E}}(t)|^2$. Substituting Eq. 1.58 into 1.55

$$\frac{\partial^2 \tilde{\mathbf{P}}_\alpha}{\partial t^2} = \frac{n\hbar\omega_0}{I_0}\frac{\partial^2 \rho}{\partial t^2}\tilde{\mathbf{E}} \tag{1.59}$$

or, in terms of the nonlinear polarization envelope in the frequency domain,

$$-(\Omega + \omega_0)^2 p_\alpha = FT\left[\frac{n\hbar\omega_0}{I_0}\frac{\partial^2 \rho}{\partial \tau^2}A\right], \tag{1.60}$$

which represents our current numerical approach. To summarize, the nonlinear polarization envelope or Eq. 1.51 is

$$\tilde{p} = 3\widetilde{\overline{\chi}}^{(3)}|A(\Omega)|^2 A(\Omega) - \frac{i\, n\hbar\omega_0}{(\Omega + \omega_0)^2} FT\left[\frac{A}{I_0}\frac{\partial^2 \rho}{\partial \tau^2}\right]. \tag{1.61}$$

1.2.2 The Current Density Envelope j and the NEE

We use, as is traditionally done, the Drude model for an electron gas:

$$\tilde{\mathbf{v}}(t) = \int_{-\infty}^{t} \frac{-e}{m}\tilde{\mathbf{E}}(t')e^{\frac{t'-t}{\tau_c}}\, dt' \tag{1.62}$$

where $\tilde{\mathbf{v}}(t)$ is the electron velocity, m is the mass of the electron, and τ_c is the average time between electron collisions. This can be represented as a convolution in the time-domain,

$$\tilde{\mathbf{v}}(t) = \frac{-e}{m}\tilde{\mathbf{E}}(t) \otimes e^{\frac{-t}{\tau_c}}, \tag{1.63}$$

so that taking the Fourier Transform and substituting

$$\tilde{\mathbf{v}}(\omega) \quad = \quad \frac{-e}{m}\frac{\tilde{\mathbf{E}}(\omega)}{\frac{1}{\tau_c} - i\omega}, \tag{1.64}$$

we have an equation for the current density, $\tilde{\mathbf{J}} = -e\rho\tilde{\mathbf{v}}$. Simplifying for the current density envelope,

$$j(\Omega) = \frac{e\rho\tau_c}{m}\frac{A(\Omega)}{1 - i(\Omega + \omega_0)\tau_c}, \tag{1.65}$$

We would like this term in the time-domain, and would like to calculate higher-order dispersion effects due to the frequency-dependence of this term. Different approaches in the literature lead to subtly different results, and here, we calculate the polarization envelope as a quasi-expansion the frequency domain,

$$j(\tau) \approx \quad FT^{-1}\left[j(\Omega = 0) + \frac{\partial j(\Omega)}{\partial\Omega}\bigg|_{\Omega=0}\Omega\right] \tag{1.66}$$

$$\approx \quad \frac{e\tau_c}{m}FT^{-1}\left[\frac{A(\Omega)}{1-i\omega_0\tau_c} + \frac{-i\tau_c A(\Omega)\Omega}{(1-i\omega_0\tau_c)^2}\right]\rho \tag{1.67}$$

$$\approx \quad \frac{e\tau_c}{m}\left[\frac{A(\tau)}{1-i\omega_0\tau_c} - \frac{\tau_c}{(1-i\omega_0\tau_c)^2}\frac{\partial A}{\partial\tau}\right]\rho. \tag{1.68}$$

Equation 1.68 makes the approximation that the spectrum of the our pulse is approximately flat, which is not necessarily accurate, particularly when pulse-splitting occurs and the spectra is consequently modulated. However, this provides a first-order dispersion correction to the current density.

We return to Eq. 1.49, collect coefficients, transform to the time-domain,

$$FT^{-1}[\Omega + \omega_0] = \omega_0(1 + \frac{i}{\omega_0}\frac{\partial}{\partial_\tau}), \tag{1.69}$$

and simplifying coefficients,

$$\frac{\partial}{\partial\zeta}A = \frac{i}{2k_0}(1+\frac{i}{\omega_0}\frac{\partial}{\partial\tau})^{-1}\nabla_\perp A - \frac{2i\pi}{c^2}(1+\frac{i}{\omega_0}\frac{\partial}{\partial\tau})|A|^2A + \frac{2\pi}{c^2}\frac{n\hbar\omega_0}{I}\frac{\partial^2\rho}{\partial\tau^2}A - \frac{2\pi}{\omega_0 c}\frac{e\tau_c}{m}\left[\frac{A(\tau)}{1-i\omega_0\tau_c} - \frac{\tau_c}{(1-i\omega_0\tau_c)^2}\frac{\partial A}{\partial\tau}\right]\rho + i\frac{k_2}{2}\frac{\partial^2}{\partial\tau^2}A. \quad (1.70)$$

In chapter 3, the normalized nonlinear propagation equation that we use to model the evolution of the electric-field amplitude $A(r,\tau,z)$ for the case of a radial symmetry in a transparent medium is,

$$u_\zeta = \frac{i}{4}T^{-1}\nabla_\perp^2 u - \frac{iL_{df}}{2L_{ds}}u_{tt} + T\frac{iL_{df}}{L_{nl}}|u|^2u - \frac{L_{df}}{2L_{mp}}\frac{\eta_t u}{|u|^2} - \frac{iL_{df}}{L_{pl}}(1-\frac{i}{\omega_0\tau_c})\left[u - \frac{\frac{\tau_c}{\tau_p}u_t}{1-i\omega_0\tau_c}\right]\eta, \quad (1.71)$$

where $u(\rho,t,\zeta) = A(r,\tau,z)/A_0$ is the electric field amplitude envelope initially centered at angular frequency ω_0 and normalized by $A_0 = A(r=0,\tau=0,z=0)$, $\rho = r/w_0$, $\zeta = z/2L_{df}$, $L_{df} = k_0w_0^2$ is the diffraction length or confocal parameter, $k_0 = 2\pi n_0/\lambda$, $t = (\tau - k_1z)/\tau_p$ is the retarded time, and the operator $T = (1+i\partial_t/\omega_0\tau_p)$ follows from the slowly-varying envelope approximation. The dispersion length is $L_{ds} = \tau_p^2/k_2$, $L_{nl}^{-1} = \alpha P_{pk}/2P_{cr}$, P_{pk} is the initial peak power, and the critical power for self-focusing is defined $P_{cr} = \alpha\lambda^2/4\pi n_0n_2$ where n_2 is the nonlinear refractive index coefficient and $\alpha = 1.8962$ is a constant associated with the initial gaussian beam profile [35]. The first term in Eq. 1.71 represents linear diffraction with the inclusion of space-time focusing. The second term accounts for dispersion $k(\omega) = k_0 + k1(\omega-\omega_0) + k_2(\omega-\omega_0)^2$ and the third term describes self-steepening.

The dimensionless plasma density is scaled by the laser-induced breakdown (LIB) threshold, $\eta = \rho/N_0$ where $N_0 = \beta^{(m)}I_0^m\tau_p/m\hbar\omega_0$, where I_0 is the gas-specific and pulse-duration dependent LIB intensity [32], and $\beta^{(m)}$ is the Keldysh coefficient [59]. We define the m-photon absorption length as $(L_{mp})^{-1} = \beta^{(m)}I_0^{(m-1)}$

and the plasma length as $(L_{pl})^{-1} = \sigma_0 N_0 / 2n_0^2 \omega_0 \tau_c$. We assume a constant inverse bremsstrahlung cross-section derived in [31] so that $\sigma_0 = \sigma(\omega_0) = k_0 \omega_0 \tau_c / [N_p(1 + (\omega_0 \tau_c)^2)]$. $N_p = m_e \omega_0^2 / 4\pi e^2$ is the electron plasma density when the plasma frequency equals ω_0. The last term of Eq. 1.71 in square brackets is a first-order chromatic dispersion correction. It is assumed that recombination and avalanche ionization effects occur at picosecond timescales [102] and can be neglected so that the nondimensionalized plasma density η is entirely formed by m-photon ionization,

$$\eta_t = \frac{\partial \eta}{\partial t} = |u|^{2m}. \tag{1.72}$$

CHAPTER 2

ANGULAR MOMENTUM AND OPTICAL VORTICES

The angular momentum density of an electromagnetic field is classically-defined as the cross-product between radius and momentum, yet its property derives entirely from coherent phase and polarization effects. Spin angular momentum (SAM) is associated with circular polarization [7]. Optical vortices with orbital angular momentum [95] reveal new dimensions of complexity in nonlinear beam propagation. These helical-phase beams have a strictly zero amplitude at the singularity where the phase is undefined and a topological charge m that is a measure of the phase winding. Fundamental research involving OAM and SAM explores quantum, nonlinear, and classical phenomena with applications in quantum cryptography, microparticle manipulation, optical switching, solitons, and remote sensing [23]. In this introduction to the angular momentum of light for studying transverse nonlinear dynamics, we provide equations for evaluating the SAM and OAM density in electric fields in the paraxial limit.

The electric and magnetic fields of a continuous-wave circularly-polarized mode with transverse amplitude $A(r,\theta)$ are

$$\tilde{\mathbf{E}} = [A\hat{\boldsymbol{\sigma}}_{\pm} - \Delta_{\pm}\hat{\boldsymbol{k}}]e^{-i(\omega t - kz)}, \tag{2.1}$$

$$\tilde{\mathbf{B}} = [\mp i\mathbf{E} - \bar{\boldsymbol{\sigma}}_{\mathbf{2}}(\nabla_{\perp}\Delta_{\pm})]e^{-i(\omega t - kz)}, \tag{2.2}$$

where the transverse gradient is $\nabla_{\perp} = \nabla - \partial_z\hat{\boldsymbol{k}}$, the second spin-Pauli matrix is $\bar{\boldsymbol{\sigma}}_{\mathbf{2}}$, and the orthogonal unit vectors associated with each circular polarization are $\hat{\boldsymbol{\sigma}}_{\pm} = (\hat{\boldsymbol{i}} \pm i\hat{\boldsymbol{j}})/\sqrt{2} = (\boldsymbol{r} \pm i\hat{\boldsymbol{\theta}})e^{\pm i\theta}/\sqrt{2}$. Substituting $\nabla_{\perp}$ and $\hat{\boldsymbol{\sigma}}_{\pm}$, Maxwell's equations require that the magnitude of the longitudinal field component is

$$\Delta_{\pm} = \frac{i}{k}\nabla_{\perp} \cdot A\hat{\boldsymbol{\sigma}}_{\pm} \tag{2.3}$$

$$= \frac{i}{k}[(\partial_r + \frac{1}{r})\boldsymbol{r} + \frac{\partial_\theta}{r}\hat{\boldsymbol{\theta}}] \cdot A[e^{\pm i\theta}\boldsymbol{r} \pm ie^{\pm i\theta}\hat{\boldsymbol{\theta}}] \tag{2.4}$$

$$= \frac{i}{k}[(\partial_r A) \pm i\frac{\partial_\theta}{r}A]e^{\pm i\theta}. \tag{2.5}$$

This representation of the longitudinal field component [Eq. 2.5] illustrates two important characteristics of circularly-polarized fields. The magnitude of this longitudinal field component depends on the radial and azimuthal gradients, which add or cancel depending on the polarization handedness. Furthermore, the complex-valued electric-field longitudinal component experiences unit addition or subtraction of a topological charge depending on the handedness of the circular polarization, due to the cylindrical-coordinate representation of circularly-polarized fields.

To evaluate fields in the paraxial limit, we neglect the second term of the magnetic field in Eq. 2.2, which scales with second-order derivatives of A and k^{-1}. The longitudinal component of the classically-defined angular momentum vector of a circularly-polarized electromagnetic field is

$$< J_z > = \frac{1}{8\pi c}[\mathbf{r} \times (\mathbf{E} \times \mathbf{B}^*) + c.c.]_z \tag{2.6}$$

$$= \frac{r}{8\pi c}\boldsymbol{r} \times \{(A\hat{\boldsymbol{\sigma}}_\pm - \Delta_\pm\hat{\boldsymbol{k}})$$

$$\times[\mp iA^*\hat{\boldsymbol{\sigma}}_\mp \pm i(\Delta_\pm)^*\hat{\boldsymbol{k}}] + c.c.\}_z. \tag{2.7}$$

Since $\hat{\boldsymbol{\sigma}}_\pm \times \hat{\boldsymbol{\sigma}}_\mp \propto \hat{\boldsymbol{k}}$ and $\hat{\boldsymbol{k}} \times \hat{\boldsymbol{k}} = 0$, only the two cross-terms between $\hat{\boldsymbol{\sigma}}$ and $\hat{\boldsymbol{k}}$ contribute to $< J_z >$. Using a common vector identity,

$$< J_z > = \frac{\pm ir\boldsymbol{r}}{8\pi c} \times \{[A\hat{\boldsymbol{\sigma}}_\pm] \times (\Delta_\pm)^*\hat{\boldsymbol{k}}) + c.c.\}_z \tag{2.8}$$

$$= \frac{\mp ir}{8\pi c}[A\Delta_\pm^*(\hat{\boldsymbol{\sigma}}_\pm \cdot \boldsymbol{r})\hat{\boldsymbol{k}}) + c.c.]_z \tag{2.9}$$

$$= \frac{\pm r}{8\pi c\sqrt{2}k}\{A[(\partial_r A^*) \mp i\frac{\partial_\theta}{r}A^*] + c.c.\}, \tag{2.10}$$

where we divide the radial and azimuthal components, commonly associated with spin angular momentum and orbital angular momentum, in the following

manner:

$$< S_z > = \frac{\pm r}{8\pi c\sqrt{2}k} A(\partial_r A^*) + c.c. \tag{2.11}$$

$$< L_z > = \frac{-i}{8\pi c\sqrt{2}k} A(\partial_\theta A^*) + c.c., \tag{2.12}$$

which is consistent with former analyses [2, 3]. Equations (2.11) and (2.12) underline how SAM and OAM are related through symmetry but also represent vectorial corrections to scalar equations. We now apply our formalism towards understanding spin-polarized fields propagating in isotropic nonlinear Kerr self-focusing media.

2.1 Collapse of Optical Vortices

Here we investigate the collapse of optical vortices in self-focusing Kerr media. Soliton vortex dynamics have been theoretically investigated in numerous contexts [23, 65], and the angular momentum and spatial dynamics have been studied experimentally in de-focusing Kerr, photorefractive, quadratic, and saturable nonlinear media [23, 29]. Some evidence of vortex MF in self-focusing Kerr media has been observed [40], however these preliminary experiments were with powers below the critical threshold for vortex ring collapse.

In contrast to the MF of vortex rings in saturable media where an m-charge vortex tends to $2m$ filaments [8], we find filamentation in a purely Kerr medium to be a function of both input power and m. We derive a new analytical relation that predicts the number of filaments which is in agreement with numerical simulations. Furthermore, we perform, to our knowledge, the first experimental study of *collapsing* vortices in Kerr media, the results of which are in excellent

agreement with our predictions. The radially-symmetric self-similar collapse of these beams, investigated previously [65] is performed via a different formalism [36], and we show the agreement between simulation and analytical curves. Our analysis extends the previous work of vortex azimuthal MI [96, 104].

A radially-symmetric field with topological charge m will approach a specific self-similar shape in a manner analogous to the evolution of $m = 0$ beams to the Townes profile [14, 77]. The critical power for vortex ring collapse for a Laguerre-Gaussian with vortex charge m can be approximated as [65]

$$P_{cr}^{(m)} = \frac{2^{2m+1}\Gamma(m+1)\Gamma(m+2)}{2\Gamma(2m+1)} P_{cr}. \tag{2.13}$$

Regardless of the initial shape, for powers above a critical threshold, the collapsing portion of the beam converges towards a distinct profile, in which the peak intensity scales inversely with the width, while the remaining portion diffracts. This self-similar profile ψ_{norm} thus has the form $\psi(\zeta,\rho,\theta)_{norm} = L(\zeta)\psi\left(\zeta, \frac{\rho}{L(\zeta)}, \theta\right)$, where $L(\zeta) = \frac{1}{max|\psi|}$. We define $\tilde{Y}_{m,P}$ to be the profile to which $\psi(\zeta,\rho,\theta)_{norm}$ is asymptotic as ζ tends to ζ_c, which is the normalized distance at which ψ becomes singular. To find $\tilde{Y}_{m,P}$ analytically, we use a general lens transformation for solutions of self-similar type near collapse [36], assume $L(\zeta) \sim \sigma\sqrt{\zeta_c - \zeta}$, and find that $\tilde{Y}_{m,P}$ obeys the equation

$$\tilde{Y}'' + \frac{1}{\tilde{\rho}}\tilde{Y}' - \left[m^2/\tilde{\rho}^2 - \sigma^4\tilde{\rho}^2 + 4\right]\tilde{Y} + \frac{2\alpha\pi P}{P_{cr}}\tilde{Y}^3 = 0, \tag{2.14}$$

where $\tilde{\rho} = \frac{\rho}{L(\zeta)}$ is the normalized radius and $\tilde{Y}(\tilde{\rho}=0) = \tilde{Y}(\tilde{\rho}=\infty) = 0$. The Townes profile is equivalent to $\tilde{Y}_{m,P}$ with $m = 0$, $\sigma = 0$, and $P = P_{cr}$. In Fig. 2.1 we plot $\tilde{Y}$ for different m and P, determined by employing a shooting method, beginning close to zero and minimizing the power at a radius ten times that of the peak field, fixing σ for a solution with unit power, and finally renormalizing the result

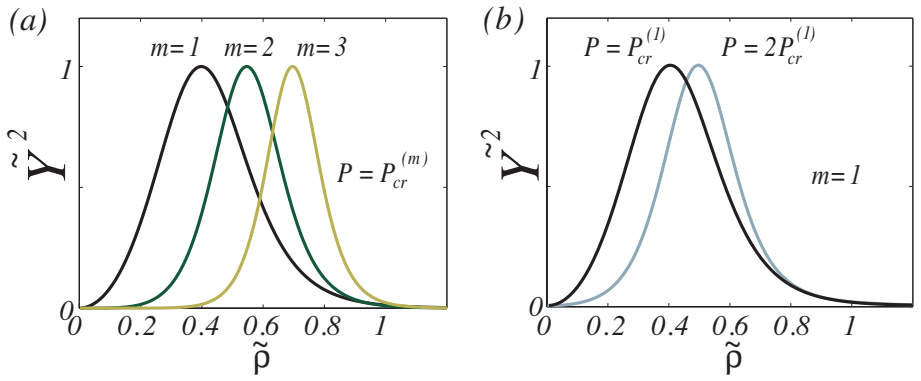

Figure 2.1: Self-similar profiles $\tilde{Y}_{m,P}$ with (a) $P = P_{cr}^{(m)}$ and $\sigma = 0.47$ for $m = 1, 2$, and 3 (b) $P = 4P_{cr} \approx P_{cr}^{(1)}$ and $P = 8P_{cr} \approx 2P_{cr}^{(1)}$, corresponding to $\sigma = 0.47$ and $\sigma = 0.38$, respectively, for $m = 1$.

so that the peak field amplitude is 1. Thus, $\tilde{Y}_{m,P}$ are the unique solutions of Eq.(2.14) defined by m and P, with power and maximal norm of 1.

In Fig. 2.2 we plot the evolution of a Laguerre-Gaussian input field with a topological charge of $m = 1$ and $P = 4.4P_{cr} \approx 1.1P_{cr}^{(1)}$. After propagating $\zeta = 0.5$, the intensity of ψ_{norm} above the $1/e^2$ point is nearly identical to the $\tilde{Y}$-profile. The ring intensity continues to increase and correspondingly shrink in both diameter and thickness as its normalized profile converges to $\tilde{Y}$. The relatively wide sampling of [4096x4096] points for $\rho = [-20, 20]$ in the split-step numerical computation, along with a super-gaussian transmission window ensure that numerical noise and reflected power do not prematurely seed vortex breakup or cause vortex transmutation [33], and a nonuniform propagation stepsize minimizes simulation error. Similar convergence to $\tilde{Y}$ can be demonstrated with other radially-symmetric input profiles of varying m and P.

The addition of azimuthal noise alters collapse to a self-similar ring profile, and instead we observe breakup into a ring of individual filaments and investigate these MF patterns. Due to the on-axis phase singularity where

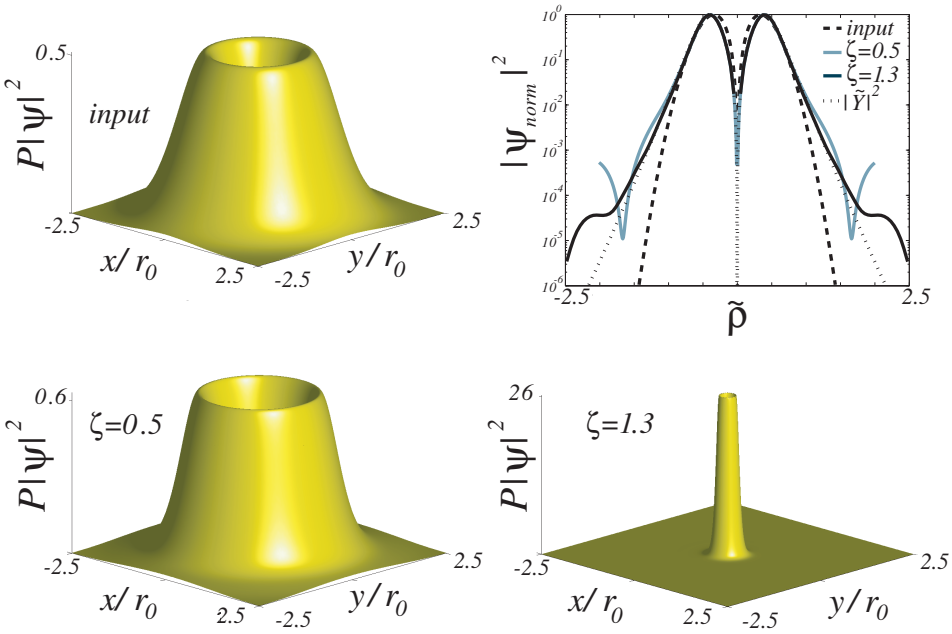

Figure 2.2: Simulation plots for an input $\tilde{LG}_{0,1}$ with $P = 4.4P_{cr} \approx 1.1P_{cr}^{(1)}$ at $\zeta = 0$, 0.5, and 1.3. Surface plots of $|\psi|^2$ are shown with the vertical axis scaled by P. Intensity cross-sections of ψ_{norm} are drawn for the input (dashed), profiles at $\zeta = 0.5$ and 1.3 (solid), and the $\tilde{Y}$ to which ψ_{norm} converges (dotted). The intensity at $\tilde{\rho} = 0$, which is equal to zero, is not shown.

the field is strictly zero, optical vortex beams result in the formation of filaments off-axis. For our perturbation analysis, instead of plane waves [96] or uniform-intensity rings [104], we use stationary field amplitudes resembling the Laguerre-Gaussian $TEM_{p,l}$ modes, with the radial mode index $p = 0$, the azimuthal index $l = m$, such that

$$\psi(\zeta, \rho, \theta) = C(1 + \delta)\, \tilde{LG}_{0,m}(\rho, \theta), \tag{2.15}$$

$$\tilde{LG}_{0,m}(\rho, \theta) = (\frac{\rho}{w})^m e^{-\frac{1}{2}(\frac{\rho}{w})^2} e^{im\theta}, \tag{2.16}$$

where C and w are the normalization terms for the electric field amplitude and mode field, respectively, and δ is the phase perturbation of azimuthal wavenum-

ber η,

$$\delta = \delta_1(\zeta)e^{i\eta\theta} + \delta_2(\zeta)e^{-i\eta\theta}. \tag{2.17}$$

We assume the instability occurs at the radius of maximum intensity and sub-

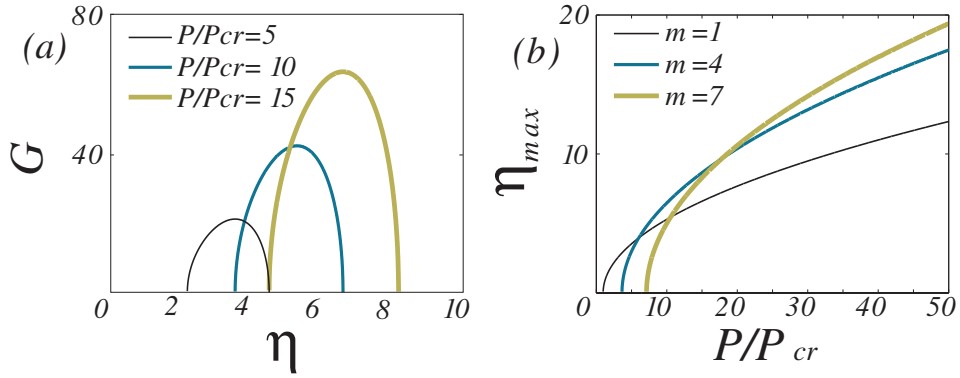

Figure 2.3: (a) Gain G of the azimuthal instability as a function of wavenumber η for $m = 1$, $P = 5P_{cr} \approx 1.25P_{cr}^{(1)}$, $10P_{cr} \approx 2.5P_{cr}^{(1)}$, and $15P_{cr} \approx 3.75P_{cr}^{(1)}$. As the power increases, G shifts to higher values of η. (b) Plot of the maximum-gain η as a function of P/P_{cr} for $m = 1, 4$, and 7.

stitute $\rho = \sqrt{m}w$. We look for solutions to $\delta_1(\zeta)$ and $\delta_2(\zeta)$ in the form of $e^{G\zeta}$, where G has a non-vanishing real part, and identify the relation for G,

$$G = \frac{(m + \frac{1}{2})}{m}\sqrt{\tilde{P}_m^2 - (\mu - 2\tilde{P}_m)^2}, \tag{2.18}$$

where $\tilde{P}_m = \frac{2P\alpha m^m}{P_{cr}e^m}$ and $\mu = 2m + m^2 + \eta^2$. The wavenumbers η which satisfy Eq. (2.18) for positive G will experience gain as plotted in Fig. 2.3(a). As the power increases, G becomes wider and taller. As the power or topological charge increases, G shifts towards higher η. It follows immediately from Eq.(2.18) that the maximum G is attained at $\mu = 2\tilde{P}_m$ and is equal to $G_{max} = \frac{2(m+\frac{1}{2})P\alpha m^{m-1}}{P_{cr}e^m}$ from which we can extrapolate that at higher powers, vortices with higher topological charge are more susceptible to azimuthal MI. This relation for G_{max} yields the following prediction for the number of azimuthal maxima in the MF patterns for

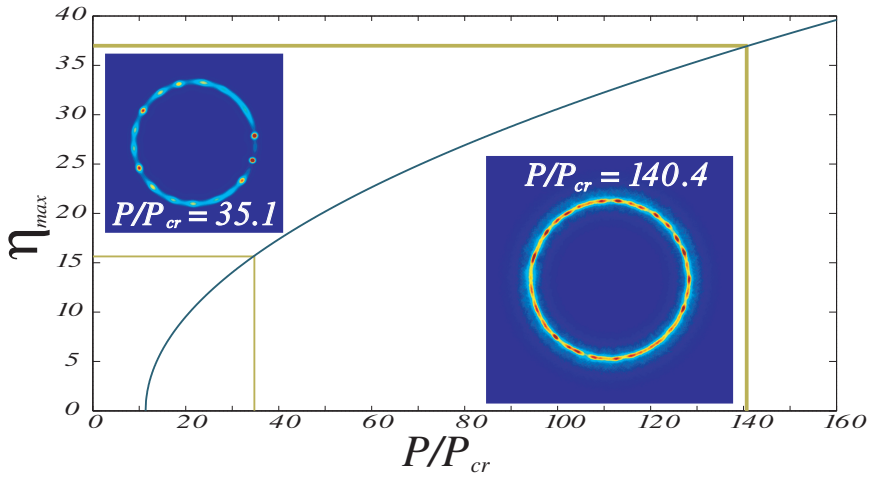

Figure 2.4: Numerical and analytical results for topological charge $m = 10$. The curve plots the wavenumber η_{max} of maximal gain as a function of P/P_{cr}. The left inset shows the MF pattern of $P = 35P_{cr} \approx 0.56P_{cr}^{(10)}$ at $\zeta = 0.07$ from numerical simulations with 16 azimuthal maxima. The right inset shows that for $P = 140P_{cr} \approx 2.24P_{cr}^{(10)}$ and 36 azimuthal maxima at $\zeta = 0.02$. In both cases the analytical predictions are in excellent agreement with the simulation results.

a given value of P

$$\eta_{max} = \sqrt{2\tilde{P}_m - 2m - m^2}. \tag{2.19}$$

Thus, we can approximate the wavenumber of maximal gain and the MF patterns solely as functions of beam power and topological charge. Plots for η_{max} as a function of P for m=1, 4, and 7 are shown in Fig. 2.3(b). We verified our model with the numerical code used to demonstrate self-similar collapse, and using 10% amplitude and phase noise, we find that our simulations match Eq.(2.19) for a topological charge up to at least $m = 10$ (see Fig. 2.4). Our work is consistent with recent analysis [104], predicting $2m + 1$ azimuthal maxima at $P = P_{cr}^{(m)}$. Moreover, our theory utilizes an integrable analytic field, the result of which is independent of ring radius and valid for powers other than $P_{cr}^{(m)}$.

Above $P_{cr}^{(m)}$, numerical simulations confirm the analytical prediction from

Eq.(2.18) that higher-charge vortices are increasingly susceptible to azimuthal MI since MF occurs at shorter normalized distances for comparable noise and powers. At lower powers, spatial spreading results in higher stability to azimuthal MI [40]. We observe in our simulations that a vortex of $m = 10$ and $P = 20P_{cr} \approx 0.3P_{cr}^{(10)}$ with 5% noise neither forms azimuthal maxima nor collapses but instead diffracts as a ring. We find, however, the same $m = 10$ vortex with 20% noise forms 10 filaments in agreement with analytical predictions. Our perturbation analysis utilizing a stationary profile accurately describes the MF of Laguerre-Gaussian beams for powers below $P_{cr}^{(m)}$, and for powers above $P_{cr}^{(m)}$, when breakup caused by MI is seeded initially. Under conditions where the vortex is more stable to MI and approaches the $\tilde{Y}$-profile before undergoing filamentation, our prediction for the number of filaments may become less accurate.

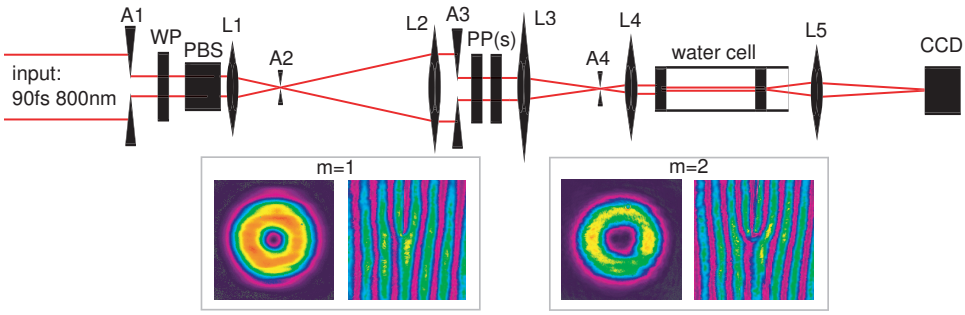

Figure 2.5: Experimental setup. The half-wave plate WP and polarizing beam splitter PBS control the power. In the spatial filter L1-A2-L2, aperture A2 is a high-power tungsten pinhole. Aperture A3 selects a small portion of the gaussian beam to transmit through the spiral phase plate(s) PP. Aperture A4 filters out higher-order Laguerre-Gaussian modes. The lower insets show typical transverse profiles incident upon the water cell and branching interference fringes demonstrating the vortex phase. The fringes are produced using a continuous-wave beam at 800nm and by imaging the phase plate(s) with a gaussian beam of zero topological charge.

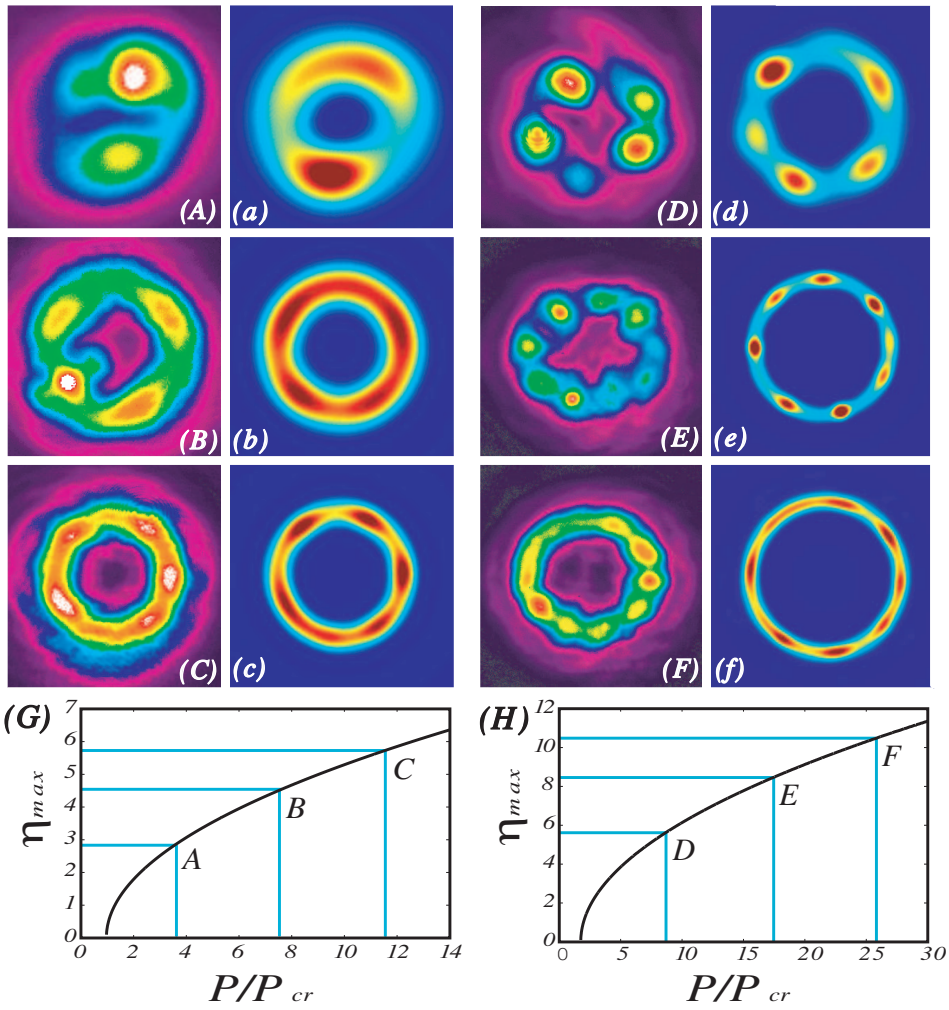

Figure 2.6: Experimentally observed output profiles for $m = 1$ with pulse energies (A) $6\mu J$, (B) $12\mu J$, (C) $18\mu J$, and corresponding simulations with powers (a) $P = 3.85P_{cr} \approx P_{cr}^{(1)}$, (b) $P = 7.7P_{cr} \approx 2P_{cr}^{(1)}$, (c) $P = 11.6P_{cr} \approx 3P_{cr}^{(1)}$. Experimental pictures for $m = 2$ with pulse energies (D) $6\mu J$, (E) $12\mu J$, (F) $18\mu J$, and corresponding simulations with powers (d) $P = 8.6P_{cr} \approx 1.1P_{cr}^{(2)}$, (e) $P = 17.2P_{cr} \approx 2.2P_{cr}^{(2)}$, (f) $P = 25.8P_{cr} \approx 3.3P_{cr}^{(2)}$. Plots of η_{max} vs P/P_{cr}, with points along the curve marked to represent corresponding MF patterns shown for $m = 1$ (G) and $m = 2$ (H).

The experimental setup for investigating the collapse dynamics of optical vortices is shown in Fig. 2.5. Laguerre-Gaussian modes are produced using spiral phase plates with 90-fs, 800-nm pulses of a Ti:Sapphire regenerative am-

plifier system. The phase plates are $m = 1$ and are made from a polymer material using a high-precision molding technology [82]. Two plates are stacked to produce $m = 2$ vortices. The telescoping is changed to vary the input beam width, and the final telescoping ranges from 50:1 to 2:1 demagnification. We estimate that the pulses have slightly broadened to 100 fs after the telescoping. The vortices are propagated through an adjustable-length cell filled with water [27]. The time-averaged spatial beam profile from approximately 130 pulses is imaged with a 12-bit CCD camera (Spiricon LBA-FW-SCOR20). Distilled deionized water is used in the experiments, since it has a higher threshold for plasma formation than plain distilled water. Fig. 5 shows the typical input intensity profile and its interference pattern with a flat-phase gaussian beam. The latter shows a branch in the fringes verifying the $m = 1$ and $m = 2$ singularities produced by the phase plates.

We propagate $m = 1$ and $m = 2$ vortices until just before the point at which super-continuum generation is observed, which indicates that collapse has occurred [41], and modify the telescoping L3-L4 so that this distance to collapse is 15-20 cm. Figures 2.6(Aa-Ff) show experimental results and the corresponding simulations for $m = 1$ and $m = 2$, where doubling and tripling the power has the effect of changing the number of azimuthal maxima from 2 to 4 to 5 and from 5 to 8 to 10, respectively. These results are highly repeatable and the number of azimuthal maxima, within the propagation distances described, vary at most by one. The CCD images are also highly stable, which we attribute to the pulse-to-pulse power stability of our laser system. The primary source of noise is inhomogeneity in the beam profile due to the alignment and imperfections of the PPs and the final aperture A4. Differences between experimental and simulation images are not surprising in view of these imperfections. However,

while variations of the input profile affect the distance to collapse, the resulting η, within the lengths described, is virtually unchanged. We estimate that a $0.6\mu J$, 100 fs pulse has a peak power equal to one critical power. Our absolute power measurements are within a factor of 3 of our analytical predictions, and our relative power measurements are in excellent agreement as shown in Figs. 2.6(G-H). We believe that deviations in power from the theory are due to dispersive broadening effects that occur during propagation, which in our experiments, is responsible for a decrease in peak power of thirty percent.

In conclusion, we observe self-similar collapse of vortex beams. These beams are azimuthally unstable, and we derive an analytical expression for the number of azimuthal maxima in the breakup as a function of the power and topological charge, which predicts the MF of vortices both below and above the critical power for vortex collapse, $P_{cr}^{(m)}$. Experimental results show this trend to be reliable for optical pulses undergoing collapse with powers as high as 3 $P_{cr}^{(m)}$. Understanding MF behavior in the long-distance propagation of femtosecond laser pulses is valuable to remote-sensing applications [58]. Moreover, our results may also have relevance to vortices in Bose-Einstein condensates since the behavior of those systems has strong analogies with that of optical beams in Kerr media [23].

2.2 Orbital Angular Momentum Hall Effect via Multiple-Filamentation

The well-known Hall effect describes a spin-dependent separation of charged carriers that occurs in the presence of an applied magnetic field. More recently,

optical analogies associated with light helical phasefronts or orbital angular momentum (OAM) have been formulated [9], and this theoretical work explains how intensity patterns with different phase vorticity or topological charge experience a transverse shift upon reflection or refraction [21, 43]. The underlying physical principle is an accumulated geometric phase [5] that results from changing values of photon OAM [79], which synthesizes a larger body of work involving geometric phase and transverse shifts that are dependent on the optical spin or orthogonal-circular polarization [9, 26, 67, 85, 100].

Beyond connections with quantum mechanical phenomena, our understanding of the OAM Hall effect and geometric phase extends knowledge of a classically-defined optical angular momentum density [2, 3]. Light can impart mechanical torque via its spin polarization or via its vortex phasefronts associated with OAM. Since both spin and OAM manifest in the longitudinal components of electric fields through Maxwell's equations, spin and OAM are coupled during propagation in anisotropic materials. Methods for separately measuring either photon spin or OAM have been proposed [66] but it remains a challenge to calculate the redistribution or evolution of angular momentum [15, 71]. This has limited the previous investigations of angular momentum and geometric phase to studies of linear propagation dynamics [1] and quantized mode transformations [30, 97].

In this chapter, we describe the existence of the OAM Hall effect that occurs via multiple filamentation in isotropic nonlinear media. For the first time, we study the nonlinear dynamics associated geometric phase and electric field angular momentum and derive an analytical relation that predicts the transverse shift resulting from the growth of azimuthal instabilities at high and low

powers. The OAM Hall effect, which couples intrinsic and extrinsic OAM [84], leads to coupled geometric phases associated with spin and OAM. Our work explains experimental results observed previously [55, 108] and describes the spin-orbit interaction [67] in a formalism that draws connections between the classically-defined angular momentum of light and related quantum mechanical phenomena.

In our simulations, 10% amplitude and phase noise is added with a uniform random variable to the spatial Fourier-transform domain to create smoothly-varying aberrations in the spatial beam profile similar to those produced in experiments. Figure 2.7 illustrates the OAM Hall effect in Kerr media when the total input power is $P = 12P_{cr}$. We plot the intensity patterns of the orthogonal-polarization fields ψ_- and ψ_+ when the peak intensity has increased by a factor of 4 due to self action effects, for $m_- = +1$ and $m_+ = -1$ [Figs. 2.7(a-b)], and for $m_- = +2$ and $m_+ = -2$ [Figs. 2.7(c-d)], where $m_\pm$ are the topological charges associated with $\psi_\pm$. Green and red lines drawn through the off-axis intensity maxima of ψ_- and ψ_+ indicate that orthogonally-polarized filaments are rotated with respect to each other. The coherent superposition of the spatially-offset fields results in hybrid elliptically-polarized filaments [55, 108]. With equal input power, both the $m_\pm = \mp 1$ and $m_\pm = \mp 2$ copropagating vortices form 6 filaments, and we observe that the transverse shift is larger for higher topological charge.

To quantify the transverse shift between orthogonal-polarization filaments, we employ the recursive variational method of optical flow (VMOF) [54]. The VMOF produces a vector-field mapping between two similar images, for which we use the intensity profiles associated with the orthogonal-circular polariza-

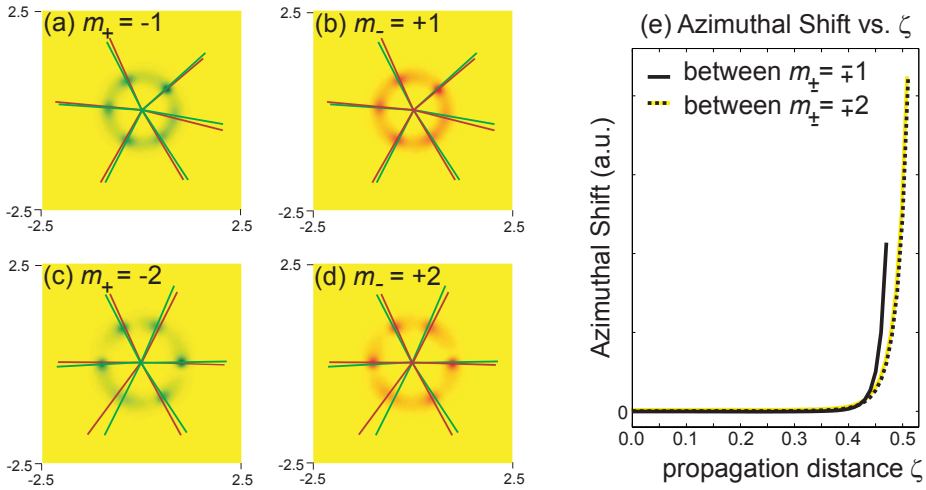

Figure 2.7: Illustration of the OAM Hall effect. Intensity profiles for orthogonal-polarization fields ψ_- and ψ_+ under self-focusing conditions when the input power $P = 12P_{cr}$ and (a-b) $m_- = +1$ and $m_+ = -1$ (c-d) $m_- = +2$ and $m_+ = -2$. Peak intensities have increased by a factor of 4. (e) Calculated azimuthal shift between ψ_- and ψ_+ intensity patterns as a function of propagation distance.

tion fields. The VMOF mapping scales in proportion to the power in the off-axis filaments and the "velocity" between the images. To compute the azimuthal shift due to the growth of the azimuthal instabilities, we sum over the azimuthal components of the VMOF mapping and divide by the peak intensity. This quantifies the transverse shift that occurs between the orthogonal-circular polarization images in relation to the distance between adjacent off-axis filaments.

In Fig. 2.7(e) we compare the azimuthal shift for copropagating ψ_+ and ψ_- vortices with topological charge $m_\pm = \mp 1$ and $m_\pm = \mp 2$ corresponding to Fig. 2.7(a-d), where we continue the numerical integration until the peak field intensity has increased by a factor of 10. Since high-power vortices are increasingly unstable to azimuthal instabilities with higher topological charge [106], we observe that azimuthal shift increases at an earlier propagation distance for $m_\pm = \mp 2$, which indicates an earlier formation of azimuthal instabilities. When

we halt the simulations, the VMOF measures that the transverse shift of $m_{\pm} = \mp 2$ as approximately twice that of the case where $m_{\pm} = \mp 1$.

In Fig. 2.8(a) we plot the azimuthal shift for copropagating ψ_- and ψ_+ vortices with topological charge $m_{\pm} = \pm 2$ for powers ranging $P/P_{cr} = 6.25$ to 18 and halt simulations when the peak intensity has increased by a factor of 10. In Fig. 2.8(b), we plot the radial position of the filaments as a function of propagation distance, and observe that for input powers $P > 8P_{cr}$, collapsing off-axis filaments have trajectories towards the origin while the azimuthal shift increases. For lower powers $P < 8P_{cr}$, the filaments travel outward while orthogonal-polarization components of each filament draw closer together, such that the azimuthal shift decreases as individual filaments undergo collapse.

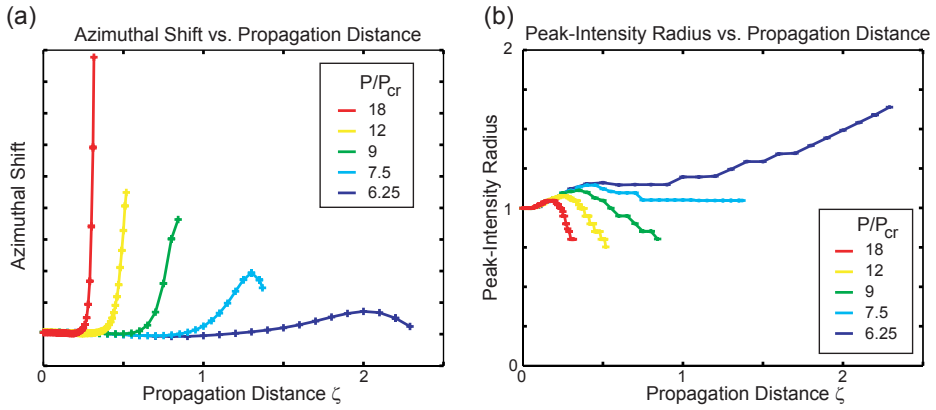

Figure 2.8: (a) Azimuthal shift between ψ_+ and ψ_- intensity patterns and the (b) radial position of maximum intensity for $m_{\pm} = \mp 2$ as a function of propagation distance for various input powers P. The transverse shift decreases when the filaments have an outward trajectory.

The underlying physical principle behind the spatial separation of vortices is the fact that persistent azimuthal modulational instabilities occur in pairs of counter-rotating waves. Although previous demonstrations of the OAM Hall effect require propagation through an inhomogeneous material it is not the

intensity-dependent refractive index, per se, that causes the spatially-rotated intensity patterns. In a manner similar to the Aharonov-Bohm effect [79], the counter-rotating waves accumulate different geometric phases, which depend on the initial field topological charge.

To analyze the spatial separation that occurs due to nonlinear dynamics, we use a separable self-similar field profile with an azimuthal perturbation of the form,

$$\psi_{\pm}(\rho,\theta,\zeta) = K(\zeta)L(\zeta)R(\frac{\rho}{L(\zeta)})e^{im_{\pm}\theta}(1+\delta_{\pm}(\theta,\zeta)), \tag{2.20}$$

where

$$\delta_{\pm}(\theta,\zeta) = \underset{2}{\delta_1}(\zeta)e^{i(\eta\theta\pm\underset{2}{\Xi_1})} + \underset{1}{\delta_2}(\zeta)e^{i(-\eta\theta\pm\underset{1}{\Xi_2})}, \tag{2.21}$$

$L(\zeta) = 1/max(|\psi|)$ when considering high-power vortices whose unperturbed propagation undergoes self-similar ring collapse, and $L(\zeta) = 1$ for assuming an unperturbed solution of a diffracting stationary profile associated with lower powers [106]. The normalization constant $K(\zeta)$ depends on δ_1 and δ_2, and the analytic form of the perturbation in Eq. 2.21 is required to conserve total OAM [2, 3]. We analyze the geometric phases $\underset{2}{\Xi_1}(\zeta)$ that accumulate during the growth of the instabilities $\underset{2}{\delta_1}(\zeta)$ of azimuthal wavenumber $\pm\eta$. When $|\delta_1|^2 - |\delta_2|^2$ is small, and in the case where copropagating orthogonal-polarization fields have opposite topological charge or $m_{\pm} = \mp m_o$, the angular shift between the orthogonal-polarization filament patterns of the Eq. 2.20 is approximately,

$$\Delta_{fil} = \Xi_1 - \Xi_2 = \int \frac{m\,L(\zeta)^2}{\rho_{fil}(\zeta)^2}d\zeta, \tag{2.22}$$

where ρ_{fil} is the radial position of the filament or azimuthal instability. The instabilities of $\exp(i\eta\theta)$ and $\exp(-i\eta\theta)$ that lead to the formation of η filaments experience a change in OAM of $m_{\pm} - \eta$ and $m_{\pm} + \eta$, respectively, which determine the position of the filaments. Orthogonal-polarization fields spatially

separate when $m_+ \neq m_-$ or during the growth of instabilities associated with inhomogeneously-polarized fields.

Our measurements of azimuthal shift in numerical simulations comparing different vortex fields $m_\pm$ [Fig. 2.7(c)] confirm that the angular shift is approximately proportional to the topological charge, as predicted by Eq. 2.22 and in Ref. [79]. Furthermore, we identify two regimes associated with the nonlinear dynamics, as shown in Fig. 2.8. Fields with power below the critical power for vortex ring self-focusing undergo diffraction where both the outward filament trajectories and cross-phase modulation reduce the OAM Hall effect and lead to decreased azimuthal shift [Eq. 2.22]. However, above the power for vortex ring self-focusing, the azimuthal shift between orthogonal-polarization vortices remains constant, since the decreasing radii of the filaments compensate for self-action effects associated with individual filament collapse.

The OAM Hall effect, which couples intrinsic and extrinsic OAM, leads to several novel propagation dynamics within the paraxial regime. We measure the exchange of *intrinsic* OAM between copropagating fields and observe that the geometric phase associated with spin and OAM can add or cancel. Local contributions of spin and OAM are determined by the transverse gradient of the spatial beam profile and calculated by $< \widehat{S}_\pm >= \pm\rho\psi_\pm(\partial\psi_\pm^*/\partial\rho) + c.c.$ and $< \widehat{L}_\pm >= -i\psi_\pm(\partial\psi_\pm^*/\partial\theta) + c.c.$ The operators $\widehat{S}_\pm = \pm\rho\partial/\partial\rho$ and $\widehat{L}_\pm = -i\partial/\partial\theta$ follow from [2, 3] and calculate the longitudinal components of the angular momentum vector in the circular-polarization basis.

In Fig. 2.9(a) we show the evolution of intrinsic OAM for various input powers P corresponding to Fig. 2.8. Through combined contributions of the OAM Hall effect and cross-phase modulation, each orthogonal-circularly polarized

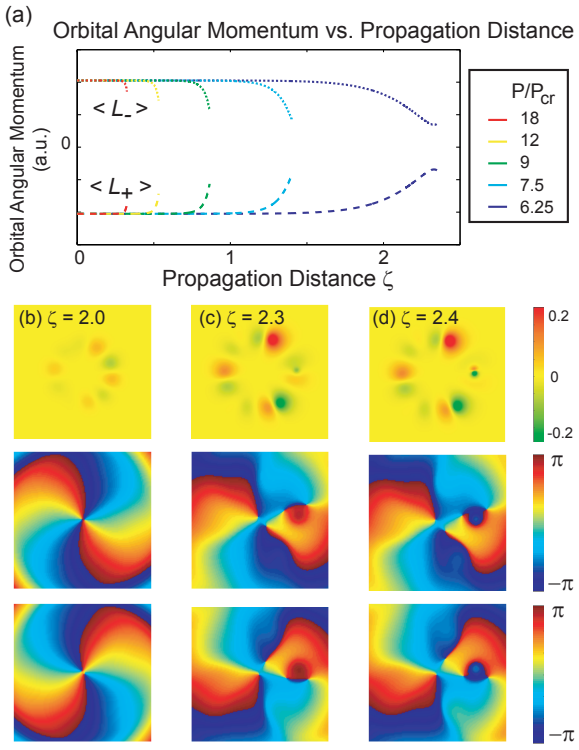

Figure 2.9: (a) Evolution of the orbital angular momentum (OAM) associated with each orthogonal-spin polarized field $\psi_{\pm}$ where $m_{\pm} = \mp 2$ for input powers corresponding with Fig 2.8. Changes in OAM are associated with the nonlinear trajectory of off-axis phase vortices. The degree of circular polarization, ψ_{+} and ψ_{-} phase profiles for $P = 6.25P_{cr}$ are shown for propagation distances (b) $\zeta = 2.0$, (c) $\zeta = 2.3$, and (d) $\zeta = 2.4$.

field experiences spatially-offset modifications of the optical refractive index. We observe that OAM exchange between orthogonal polarizations is larger for longer propagation distances and with lower input beam powers. The dynamics are accompanied by the formation, annihilation, and nonlinear trajectories of phase vortices. Dramatic changes in the phase profiles associated with ψ_{+} and $P = 6.25P_{cr}$ are shown in Figs. 2.9 (b-d), where for each figure the first row corresponds to the degree of circular polarization, or $|\psi_{+}|^2 - |\psi_{-}|^2$ or the Stokes S_3 matrix and the second and third columns represent the phase profiles of the

multiple filamentation pattern. The formation of 6 filaments cause azimuthal distortions in the phase profile as the beam diffracts [Fig. 2.8(c)], and these phase distortions form a topological defect pair between $\zeta = 0$ and $\zeta = 2.3$. At $\zeta = 2.3$, we only one of the original topological charges remains on-axis. The formation of off-axis topological defects accompanies turning OAM dynamics [Fig. 2.9(a)].

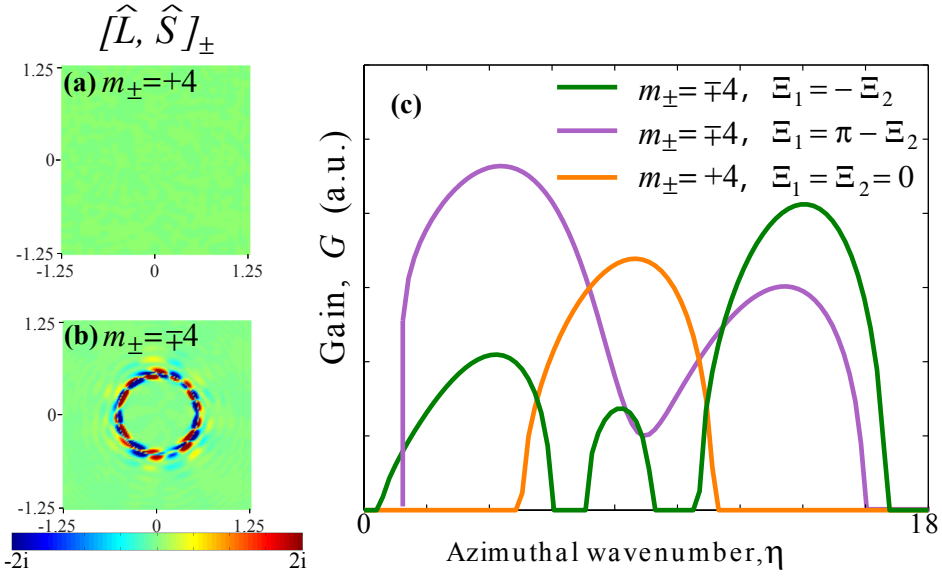

Figure 2.10: Comparison of copropagating vortices $m_{\pm} = \mp 4$ and $m_{\pm} = +4$ when the power $P = 25P_{cr}$. The spatially-varying commutator relation $[\widehat{L}, \widehat{S}]$ at $\zeta = 0.17$, is negligible when (a) $m_{\pm} = 4$ and highly corrugated when (b) $m_{\pm} = \mp 4$. (c) The gain G vs. azimuthal wavenumber η for copropagating vortices. The homogeneously-polarized case where topological charge $m_{\pm} = +4$ (orange) has one band of gain and there is no associated geometric phase. The gain associated with inhomogeneously-polarized $m_{\pm} = \mp 4$ changes depending on the geometric phase $\Xi_1 = -\Xi_2$ (green) and $\Xi_1 = \pi - \Xi_2$ (purple).

The spatial separation between copropagating vortices contributes to more complicated nonlinear propagation dynamics associated with multiple filamentation. In saturable self-focusing media, it has been shown that the interac-

tion between copropagating vortices leads to more stable soliton solutions [24]. However, we observe that in nonlinear Kerr media the OAM Hall effect leads to competition between different azimuthal instabilities associated with the changing geometric phases. We choose to illustrate this by the commutation relation between spin $\widehat{S}$ and OAM $\widehat{L}$ operators

$$[\widehat{L},\widehat{S}]_{\pm} = \left\langle \psi_{\pm} \middle| [\widehat{L},\widehat{S}] \middle| \psi_{\pm} \right\rangle = \pm i\rho \left[\frac{\partial \psi_{\pm}}{\partial \rho} \frac{\partial \psi_{\pm}^{*}}{\partial \theta} + c.c. \right], \tag{2.23}$$

which represents the accumulated geometric phase due to the effects of polarization, in agreement with the spin-orbit interaction Hamiltonian correction to the paraxial equation that was derived in [67]. The sign of $[\widehat{L},\widehat{S}]_{\pm}$ indicates whether geometric phase contributions associated with changes in spin and OAM due to torsional ray trajectories partially add or cancel. Due to the parallel transport effect [5, 9], the transverse shift in the intensity patterns is accompanied by the field advancing or receding in the $\hat{\boldsymbol{k}}$-direction depending on the orthogonal-spin polarization.

This interpretation of a commutator relation, which follows from the derivation of spin and OAM geometric phase analyzed in [9], illustrates paraxial dynamics associated with the transverse spatial beam profile. Only nonradially-symmetric spin-polarized fields carry spatial locations where $[\widehat{L},\widehat{S}]_{\pm} \neq 0$. Moreover, as in the electronic analogy, we observe that it is possible for an electric field to carry both zero net spin and zero net OAM, but have a nonzero commutator relation where $[\widehat{L},\widehat{S}]_{+} + [\widehat{L},\widehat{S}]_{-} \neq 0$. The OAM Hall effect provides the interaction for observing this relation precisely during the multiple filamentation of two orthogonal circularly-polarized nonradially-symmetric fields $\psi_{\pm}$, where $m_{\pm} = \mp m_o$.

In Figs. 2.10(a-b) we compare the spatially-varying commutator relation

$[\widehat{L},\widehat{S}]_{\pm}$ of multiple filamentation patterns for homogeneously-polarized $m_{\pm} = 4$ and inhomogeneously polarized $m_{\pm} = \mp 4$ copropagating vortices. Although both conditions result in the formation of 8 collapsing off-axis filaments, at the propagation distance $\zeta = 0.17$ when the peak intensity has increased by a factor of 5, the commutator relation varies drastically. As expected, we observe negligible coupling between spin and OAM geometric phases for the case where $m_{\pm} = 4$, since there is no spatial separation between orthogonal-polarization fields [Fig. 2.10(a)]. In contrast, the commutator relation $[\widehat{L},\widehat{S}]_{\pm}$ for the inhomogeneously-polarized case illustrates a irregularly-corrugated and spatially-varying coupling between spin and OAM geometric phases.

We calculate the gain G associated with the growth of azimuthal instabilities as a function of the azimuthal wavenumber η to explain the irregular azimuthal modulations in spatial beam profile illustrated by Fig. 2.10(b). Solutions for the gain G are calculated by using a similar approach as in [106] incorporating geometric phase and cross-phase modulation. For copropagating vortices where $m_{\pm} = \mp 4$, we observe multiple bands of gain depending on the geometric phase. We plot different solutions for the gain for different values of geometric phase $\Xi_1 = -\Xi_2$ (green) and $\Xi_1 = \pi - \Xi_2$ (purple) and compare with the gain curve associated with $m_{\pm} = 4$, which is unchanged by geometric phase (orange). The widened gain and growth of numerous wavenumbers indicate competing dynamics between azimuthal instabilities. In simulations involving inhomogeneously-polarized fields we observe turbulent dynamics during the initial stages of propagation, which are explained by shifting gain curves G associated with varying geometric phases $\Xi_{\frac{1}{2}}$ and the OAM Hall effect.

In conclusion, the OAM Hall effect manifests itself during the multiple fil-

amentation of copropagating optical vortices of different topological charge in nonlinear self-focusing Kerr media. When the filaments have outward trajectories, the spatial separation is reduced by cross-phase modulation within individual filaments. At lower powers and longer propagation distances, the OAM Hall effect in combination with cross-phase modulation results in OAM exchange between orthogonal polarizations. A new commutator relation illustrates how coupled geometric phases associated with spin and OAM accompany the OAM Hall effect.

As the original electronic Hall effect is exploited in numerous applications of sensors, the separation of polarization components via the OAM Hall effect in filamentation provides a means for manipulating and interpreting the evolution of vortex fields. Our results are relevant to understanding changes in the spatial-beam profile of inhomogeneously-polarized and phase vortex beams in remote sensing, laser machining, trapping, and microscopy applications. This research draws new connections between the classically-defined angular momentum of light and quantum mechanical effects associated with spin particle dynamics.

2.3 Geometric Phase and Angular Momentum Switching between Optical Vortex Beams

In the novel "Around the World in Eighty Days" by Jules Verne, the main characters circumnavigate the globe in 1872 as part of a wager, and gain an extra "day", measured by sunrises and sunsets. Vernes characters fortuitously chose an eastward heading, for if instead they had taken a westward path, they would have crossed the international dateline in the opposite direction and forfeit the

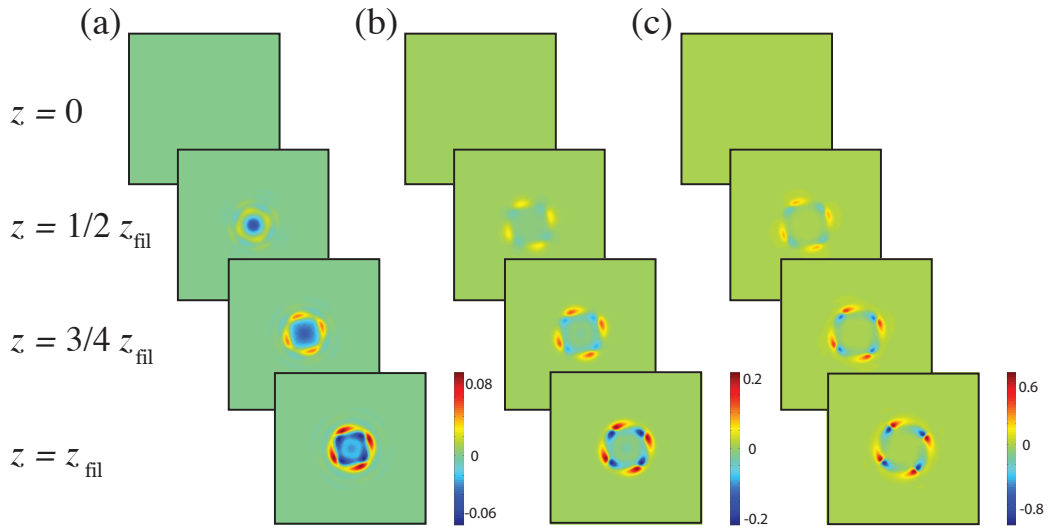

Figure 2.11: Degree of circular polarization or $|\psi_{-}^{(m)}|^2 - |\psi_{+}^{(0)}|^2$ at $z = 0, 1/2 z_{fil}, 3/4 z_{fil}, and z_{fil}$ for copropagating orthogonal-spin fields $\psi_{+}^{(0)}$ and $\psi_{-}^{(m)}$ where (a) $m = 1$ (b) $m = 3$ and (c) $m = 7$, and $z_{fil} = 0.25, 0.18$, and 0.14. The radial separation of orthogonal-spin fields is due to diffraction, while the azimuthal separation is due to the accumulated geometric phase associated with counter-rotating instabilities.

wager. The difference of one "day" that is generally experienced between eastward and/or westward travelers whose combined journeys encircle either pole, is an illustration of a path-dependent geometric phase. Geometric phase arises in a range of physical and mathematical phenomena and in quantum mechanics, it is observed by superposing two particles or waves that have taken different paths, and measuring the shift of interferometric fringes.

In our nonlinear optics investigations, the interference patterns of counter-rotating waves are the transverse intensity modulations or azimuthal instabilities, that experience growth on OPVs due to an intensity-dependent refractive index. Instabilities in the spatial beam profile lead to the formation of multiple off-axis filaments round nucleations of self-trapped light undergoing

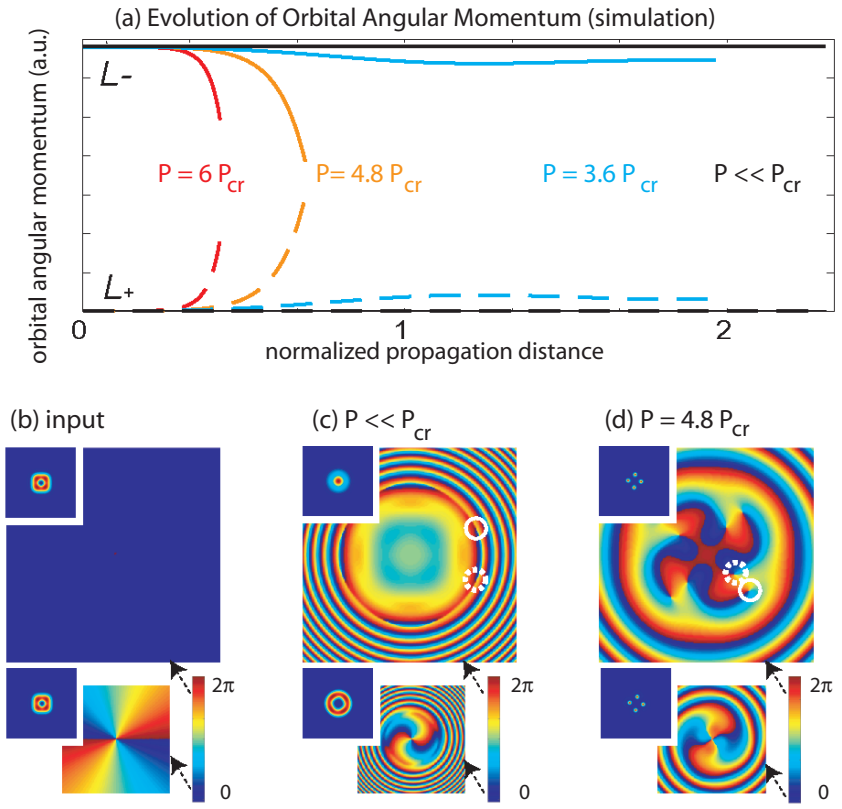

Figure 2.12: (a) Evolution of the orbital angular momentum $< L_+ >$ and $< L_- >$ associated with the optical field components $\psi_+^{(0)}$ and $\psi_-^{(2)}$, respectively, for different initial powers: diffraction or $P << P_{cr}$ (black), $3.6P_{cr}$ (blue), $4.8P_{cr}$ (orange), $6.0P_{cr}$ (red). Orbital angular momentum switching occurs between $P = 3.6P_{cr}$ and $P = 4.8P_{cr}$. Plots (b)-(d) show phase profiles for $\psi_+^{(0)}$ (above) and $\psi_-^{(2)}$ (below, scaled by half), with intensity profiles (left insets, scaled by one-third) for (b) input, (c) after propagating one diffraction length with no nonlinear interaction, and (d) with $P = 4.8P_{cr}$. In (c) and (d), the solid-circled off-axis vortex has a topological charge of 1, (clockwise red-yellow-blue), while the dashed-circled off-axis vortex has a charge of +1. (clockwise blue-yellow-red).

collapse [42] whose locations depend on the initial beam shape and power [28, 48, 106, 47], material properties and polarization effects [96, 25, 92, 87] and, as we have recently reported, an accumulated geometric phase.

Here we consider the coherent superposition of a spin-polarized OPV with topological charge m, $\psi_{-}^{(m)}$, and an identically-shaped orthogonal-spin zero-OAM ring $\psi_{+}^{(0)}$, copropagating in an isotropic self-focusing material such as water or glass. We seed multiple filamentation patterns deterministically by elongating the spatial extent of the beam 5% with 4-fold rotational geometry, which results in the formation of four filaments within the nonlinear material. The initial profiles are Laguerre-Gaussian fields, with unit radius and power normalization. We elongate the spatial extent of the transverse electric fields with perturbation parameters δ and η:

$$\psi_{-}^{(m_{-})}(\rho,\theta) = \rho^{m} e^{-\rho^{2}(1+\delta\cos(\eta\theta))} \tag{2.24}$$

where $\eta = 4$ is chosen to make the beam square-shaped in order to match our initial conditions in experiments.

In Fig. 2.11, we show the nonlinear evolution of filaments modeled with the 2D nonlinear Schrodinger equation, which takes into account diffraction, self-focusing, and cross-phase modulation. The three columns illustrate $m = 1, 3,$ and 7, with beam powers $P = 12P_{cr}$, where P_{cr} is the critical power for self-focusing of a gaussian-shaped beam. We halt simulations at z_{fil} when peak powers have increased by a factor of 4, which occurs at $z_{fil} = 0.25, 0.18, and 0.14$ diffraction lengths, respectively. Each set of plots shows the degree of spin polarization or spatial separation between orthogonal-spin components $S_3 = |\psi_{-}^{(m)}|^2 - |\psi_{+}^{(0)}|^2$ at different propagation distances, which is zero at $z = 0$.

In Fig. 2.12, we observe greater spatial separation between orthogonal-spin fields with increasing m calculated both by $\Sigma|S_3|$ and peak values of $|S_3|$. Orthogonal-spin fields separate in the radial direction due to the diffraction associated with differing phase vorticity [Fig. 2.11(a)]. Orthogonal-spin fields

also spatially separate in the azimuthal direction θ due to the growth of transverse instabilities, which are counter-rotating fields proportional to $\exp[i4\theta + \Xi_1]$ and $\exp[-i4\theta + \Xi_2]$, where $\Xi_1 - \Xi_2$ represent shifted locations or spatially-offset filaments and geometric phase. This azimuthal separation dominates in Fig. 2.11(c). We recently reported that the initial nonlinear dynamics of inhomogeneously-polarized fields are turbulent due to shifting instabilities associated with changing geometric phase, however, a more pronounced effect is OAM switching, in which each orthogonal-spin field experiences spatially-offset modifications of the optical refractive index due to cross-phase modulation, curving electric field phase fronts [1].

In Fig. 2.12, we show the evolution of the spatial beam profile and OAM associated with $\psi_+^{(0)}$ and $\psi_-^{(2)}$, or $< L_+ >$ and $< L_- >$. When there is no nonlinear interaction between $\psi_+^{(0)}$ and $\psi_-^{(2)}$, $< L_+ >$ and $< L_- >$ are unchanged. Increasing the power we observe between $P = 3.6P_{cr}$ and $P = 4.8P_{cr}$, the output OAM switches from $< L_+ > / < L_- >= 5\%$ to $< L_+ > / < L_- >= 70\%$. This transition is accompanied by a change in the spatial beam pattern, which exhibits a single on-axis peak in $\psi_+^{(0)}$ when there is low OAM exchange and off-axis filaments above the power threshold for OAM switching. At even higher powers, the filaments collapse within shorter propagation distances and with less OAM exchange [2].

The question that naturally arises is how $\psi_+^{(0)}$, which initially has no OAM,

[1] The OAM exchange was theoretically explored for coupled vortex solitons in saturable self-focusing media in [22]. We note that our definition of OAM differs from that used here, which is based on the trajectory of off-axis solitons. In contrast, our total OAM, $< L_+ > + < L_- >$, is always conserved and our analytic form measures the non-discrete change of OAM due to diffracted electric fields.

[2] If the simulations are carried further, the OAM of $\psi_+^{(0)}$ eventually exceeds that of $\psi_-^{(2)}$, however it is unclear how such numerical results would remain within paraxial assumptions, in particular, when vectorial effects are taken into account [37].

acquires the OAM that we observe. Figure 2(b) shows initial phase fronts of the co-propagating beams, $\psi_+^{(0)}$ and $\psi_-^{(2)}$ (below, at one-half scale), where the upper-left insets show the initial intensity profiles at a scale of one-third. Since there is no interaction on-axis where the beam amplitude is strictly zero due to the on-axis phase singularity of $\psi_-^{(2)}$, we expect that $\psi_+^{(0)}$ remains $m = 0$ on-axis, and that any OAM is acquired through an off-axis phase redistribution.

Fig. 2.12(c) illustrates how the input beam diffracts in the absence of any nonlinear interaction, that is, for the case $P << P_{cr}$. We see that $\psi_+^{(0)}$ and $\psi_-^{(2)}$ separate spatially within one diffraction length and four pairs of opposite-charge off-axis vortices emerge in the phase profile of $\psi_+^{(0)}$, due to the 4-fold symmetry. Although OAM is intrinsic to the helical phasefronts that constitute ring-shaped OPVs, beams do not necessarily require OAM to evolve with helical phase fronts, as pairs of opposite-charge off-axis vortices arise from the diffraction of irregularly shaped $m = 0$ beams [86, 91]. Figure 2.12(d) illustrates the nonlinear interaction effects on the phase profile for the same input beam where $P = 4.8P_{cr}$. We now find that the off-axis vortices in $\psi_+^{(0)}$ whose signs are the same as that of the acquired OAM, travel closer to the beam center. The difference in radius between the two opposite-charge off-axis vortices is representative of the OAM exchange. At higher powers, when off-axis filaments occur within shorter propagation distances, there is less OAM exchange, and the opposite-charge off-axis vortices form at smaller but comparable radii.

To demonstrate the OAM exchange experimentally, we filter out $\psi_+^{(0)}$ and $\psi_-^{(2)}$ independently and measure the off-axis trajectory of the filaments, and also study the output polarization patterns [Fig. 2.13]. We spatially and temporally overlap two pairs of Hermite Gaussian (HG) lobes consisting of 90-fs pulses at

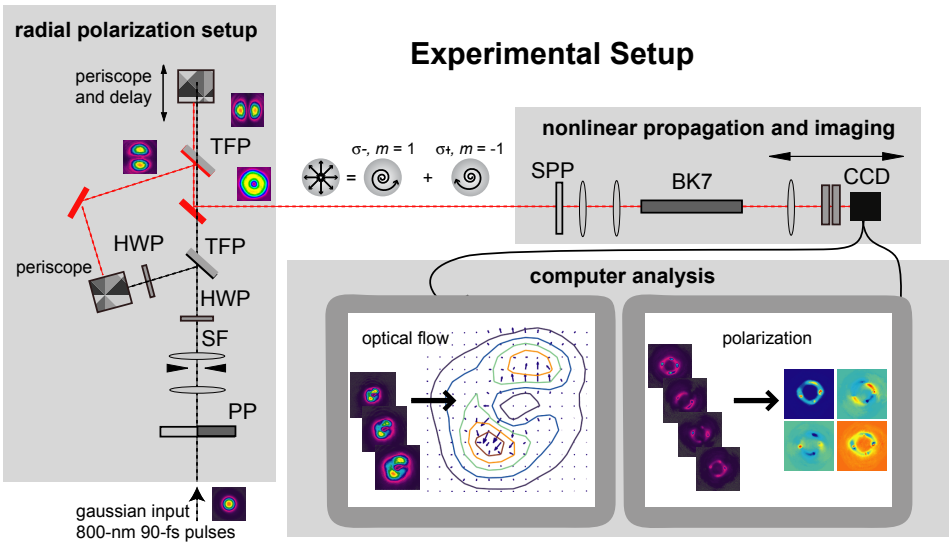

Figure 2.13: A linearly-polarized Gaussian beam is incident onto a split $0 - \pi$ - phase plate ($\pi - PP$). The beam after a spatial filter (SF) is a two-lobe Hermite-Gaussian mode. A half-wave plate (HWP) rotates the linear polarization by 45 degrees, and a thin-film polarizer (TFP) divides the beam. In one arm, an additional HWP and periscope result in a 90-degree-rotated mode. We align the two arms spatially and use a precision translation stage for temporal alignment, and verify a radially-polarized field distribution. A spiral phase plate (SPP) imprints an additional $m = +1$ topological charge, and we image the SPP onto the surface of a 30-cm-block of BK7 glass. The CCD camera takes several images of the output-filtered spin-polarized components at various distances from the output BK7 glass face, which we analyze by employing the variational method of optical flow. The CCD camera also takes four polarization-filtered images of the BK7 output face to compute the Stokes vectors.

800 nm to produce a coherent superposition of $\psi_+^{(-1)}$ and $\psi_-^{(+1)}$ Laguerre-Gaussian modes, which are square or diamond- shaped due to the imperfect aspect ratio of the HG lobes. These components are transmitted through an $m = +1$ spiral phase plate [82] that is imaged onto the surface of a 30-cm-long block of BK7 glass with varying magnification in order to investigate the dynamics for differ-

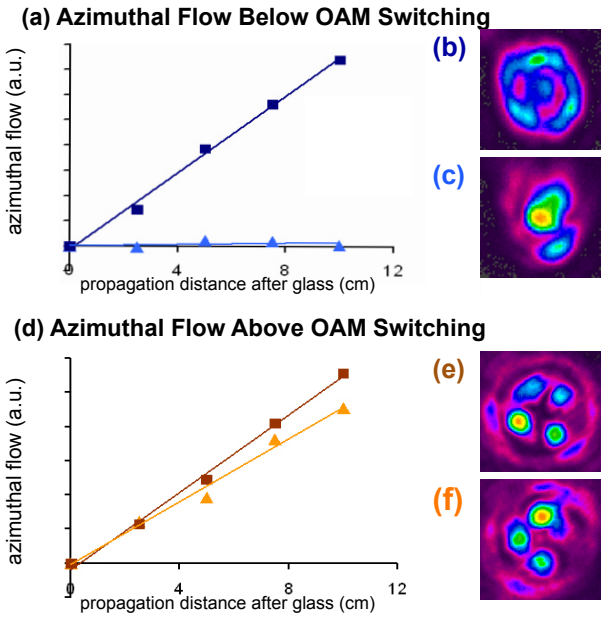

Figure 2.14: Measurements and images of the filament patterns above and below the threshold for orbital angular momentum switching. Plots of azimuthal displacement of filament patterns as a function of propagation computed by the variational method of optical flow analysis of sequential CCD images (a) below and (d) above the power threshold for OAM switching. Lines (b) and (c) show a relatively large difference in azimuthal rotation, associated with $\psi_{-}^{(2)}$ and $\psi_{+}^{(0)}$ at $P = 3\mu J$, and where the corresponding spatial beam patterns are (b) a diffracting ring, and (c) an on-axis filament. Lines (e) and (f) show comparable angular displacement when $P = 8\mu J$, where the corresponding measured spatial beam patterns show off-axis filaments. Notice, the multiple-filamentation patterns shown in Figs (e) and (f) are rotated approximately 30 degrees with respect to each other due to geometric phase.

ent input powers in the fixed glass length. We filter the $\psi_{+}^{(0)}$ and $\psi_{-}^{(2)}$ components with a broadband quarter-waveplate and a Polarcor polarizer oriented at 45 degrees to the axes of the wave plate.

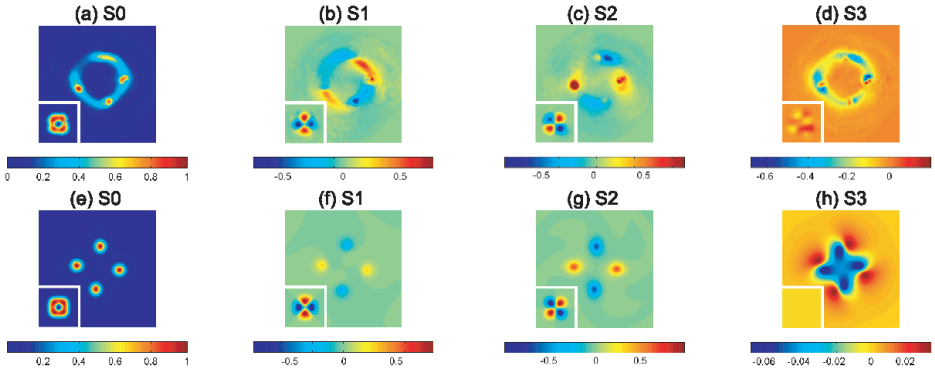

Figure 2.15: Experiment (a-d) and simulation (e-h) Stokes parameters of the output field. The inset frames show the Stokes parameters for the input. (a,e) S_0, intensity. (b,f) S_1, vertical (red) and horizontal (blue) polarizations. (c,g) S_2, 45 (red) and -45 (blue) linear polarizations. (d,h) S_3, + (blue) and (red) helical polarizations.

The filamentation patterns that form within the glass undergo diffraction in air at the output. The off-axis trajectory or azimuthal change of the patterns is a measure of the output OAM. We image the output filament patterns at 0, 2.5, 5, 7.5, and 10 cm from the BK7 output face and utilize the variational method of optical flow (VMOF) [54] to quantify and compare the small-angle rotation of $\psi_+^{(0)}$ and $\psi_-^{(2)}$ independently. The recursive VMOF produces a vector field mapping between two similar images and is highly sensitive to detecting small changes between images. To compute the azimuthal shift, we sum over the azimuthal components of the vector field mapping.

Figure 2.14 (a) and (d) show the integrated azimuthal shift or relative rotation of the beam patterns, as the undergo linear diffraction after the BK7 glass, below and above the power for OAM switching. Below switching with $P = 3\mu J$, the azimuthal shift of $\psi_+^{(0)}$ is less than 10% that of $\psi_-^{(2)}$ and we estimate that the filament patterns associated with $\psi_-^{(2)}$ rotate approximately 12 degrees within the ten-centimeter linear propagation after the output BK7 edge. Above switching

with $P = 8\mu J$, the azimuthal shift is comparable for both circular polarizations. Figures 2.14(b-c) and 3(e-f) show the experimental CCD images that correspond to the formation of on- and off-axis filaments, as also observed in simulations below and above the threshold for OAM exchange. The locations of off-axis filaments associated with $\psi_+^{(0)}$ and $\psi_-^{(2)}$ [Figs. 2.14(e-f)] are rotated with respect to eachother, a consequence of the geometric phase.

For this system of copropagating $\psi_+^{(0)}$ and $\psi_-^{(2)}$ beams, we also characterize the unique evolution of polarization patterns resulting from this nonequilibrium phase transition, in which orthogonal-polarization fields spatially separate in the linear regime simply due to diffraction [Fig. 2.12(c)]. Figure 4 shows the computed Stokes parameters for powers above OAM switching, where the insets display that for the input beam, characteristic of a radially-polarized vortex. The Stokes parameters, which show the polarization of the beam via intensity measurements, decompose the total beam [Figs. 2.15(a) and 2.15(e)] into its vertically and horizontally-polarized components [Figs. 2.15(b) and 2.15(f)], 45 and -45 linearly-polarized components [Figs. 2.15(c) and 2.15(j)], and orthogonal-spin polarizations [Figs. 2.15(d) and 2.15(h)]. It should be noted that although the Stokes parameters provide a common representation of the spatial polarization patterns, they do not provide a complete characterization of the polarization and polarization singularities .

Figures 2.15(d) and 2.15(h) illustrate the geometric phase, in which each filament has a contribution from orthogonal-circular polarizations separated spatially on either side of each filament. These regions of orthogonal spin-polarization both draw closer together as the filament collapses while also rotating around the filament, producing an observable change in the local polar-

ization. The collective dynamics pertaining to our coherent superposition of $\psi_+^{(0)}$ and $\psi_-^{(2)}$ leads to growth of azimuthally-polarized components from an initially radially-polarized beam, which can be seen in Figs. 4(c) and (f), where at the output, the top and bottom filaments have a horizontally-polarized component, and the left and right filaments have a vertically-polarized component. Simulations indicate that in the absence of temporal effects, the initially radially-polarized beam becomes more than 30% azimuthally-polarized. Furthermore, we claim that the local rotation of polarization is only observed with inhomogeneously-polarized beams with net OAM, highlighting unusual dynamics that occur via a combination of OPV diffraction and cross-phase modulation. Temporal effects account for the primary differences between simulation and experiment; the front and trailing portions of the optical pulses have lower power and experience less Kerr nonlinearity, which produces the appearance of a filament trail or background ring, as shown by the time-integrated CCD camera image.

Our experiments illuminate connections between OAM and polarization that can be interpreted in multiple ways. Cross-phase modulation provides a spin-spin coupling whose anisotropy transfers OAM from one spin polarization to the other and where the electric field vector produces an effective birefringence that leads to polarization rotation. Another perspective can be found by considering the evolution of the individual spin-polarized phasefronts, where each azimuthal instability is an extrinsic or local off-axis OAM that is coupled to the field topological charge, and where the nonlinear trajectory of off-axis vortices [Fig. 2.12(c),(d)] is a hydrodynamic effect. But we can also depict the self-focusing of the off-axis filaments as attractive bound states between orthogonal polarizations carrying different OAM, where the spin-pairs have increasingly-

similar spatial overlap and momentum as the filaments tend towards collapse. Regardless, a remarkable result is that these dynamics occur via self-induced geometrical effects in isotropic media. It is the growth of azimuthal instabilities via nonlinear self-focusing dynamics that provides asymmetry via geometric phase in a collectively-organized pattern, which couples spin angular momentum with OAM.

CHAPTER 3

SPECTRAL RESHAPING AND PULSE COMPRESSION VIA SEQUENTIAL FILAMENTATION IN GASES

Recently, filamentation has provided a mechanism for compressing pulses to only a few optical cycles with millijoule energies [50], wherein the sustained balance of self-focusing and ionization produces extensive spectral broadening. Although several other methods have demonstrated few-cycle pulse compression with energies well over a millijoule [56, 78, 94, 103], these methods require serial processes, where spectral broadening or dispersion compensation are required using separate stages. Hollow-core capillaries have been used to produce few-cycle pulse duration compression above a millijoule without the need for a secondary stage of dispersion compensation [109], however it is unclear how pulse compression could scale to higher energies in waveguiding configurations, even with large-core photonic band gap fibers [64]. Although filamentation as a mechanism for pulse compression is not without challenges, this approach appears scalable to higher pulse energies. Furthermore, recent experiments and numerical simulations demonstrate self-compression or compression without the need for additional negative dispersion compensation [93, 99].

In this chapter, we provide a theoretical description of optimal pulse compression via filamentation and we propose that the alternating dynamics between beam focusing and defocusing and the production of visible sequential plasma filaments is the primary mechanism that leads to the extensive blue-shifted spectrum which enables pulse compression. With noble gases, optimizing spectral broadening and sequential filamentation involves simply varying the gas pressure, and a distinct two-plasma-filament structure provides the vi-

sual signature of optimal spectral reshaping. While there have been extensive numerical investigations examining pressure trends [16, 17, 74, 81] and a description of serial filamentation, [13, 27, 73], to our knowledge this is the first work that ascribes the extensive spectral broadening to frequency-dependent linear and nonlinear spatial dynamics. This understanding is necessary for properly characterizing filament pulses and provides guidance for improving compression techniques.

Plasma filaments are associated with self-guiding or self-channeling of laser pulses, and only partial information can be extrapolated about the spatial or temporal profile simply by the time-integrated plasma densities. One difficulty in interpreting the nonlinear dynamics of extended filamentation is that the electric-field background reservoir, which is not directly observable in experiment, plays an enormous role in the nonlinear propagation dynamics [73]. In fact, simulations and precise measurements of meter-long single-plasma-filament densities indicate a corrugated electron-density structure [13, 89], with intermediate self-focusing stages within isolated filaments. In this paper, we refer to a filament as the presence of ionized gas or plasma, and we believe that the mechanism described here of sequential filamentation provides a building block for understanding the more complicated evolution of high-power ultrashort laser pulses.

Previous experimental results have demonstrated pulse compression via sequential filamentation with initial input pulses of 0.7 mJ at 800 nm in which initial input pulses of 35 fs were compressed to 11 fs in argon gas [52] and with 0.33 mJ pulses at 2 μm [51] from 50 fs to 18 fs in xenon. Here we show how the dynamics scale for different input pulse geometries, input pulse durations,

input pulse energies, and wavelengths, and different gas media. The goal of this paper is twofold: to provide a better framework for optimizing pulse compression via filamentation techniques and to synthesize previously published results to arrive at a more comprehensive paradigm for filamentation in gases. We provide predictions that describe how pulse compression via sequential filamentation can scale to higher pulse energies.

3.1 Compression and Pressure-dependent Sequential Filamentation at 800 nm

In this section, we consider the regime of material parameters where sequential filamentation is observed in experiments. By tuning the gas pressure, we change several physical parameters and observe trends that are repeatable under numerous experimental conditions. Although changing the pressure shifts the relative contributions of both linear and nonlinear effects in Eq. 1.71, due to the robust dynamics, sequential filamentation can still be observed within a range of input pulse powers. We also show that sequential filamentation is a template for understanding seemingly isolated and longer single plasma filaments.

The dispersion and nonlinear self-focusing coefficients scale linearly with pressure, that is,

$$\frac{L_{df}}{L_{ds}} \propto p, \tag{3.1}$$

and

$$\frac{L_{df}}{L_{nl}} \propto p, \tag{3.2}$$

since $k_2, n_2 \propto p$. The higher-order processes of plasma defocusing, multiphoton absorption, and ionization are more sensitive to changes in pressure. Since both the Keldysh rate, $\beta^{(m)}$, and LIB intensity I_0 scale linearly with pressure, it follows that the multiphoton ionization length scales to the power of m, that is,

$$\frac{L_{df}}{L_{mp}} \propto p^m. \tag{3.3}$$

The electron collision time τ_c scales inversely with pressure, and in the limit $\omega_0 \tau_c >> 1, \sigma_0 \sim 1/\tau_c$, and the inverse bremsstrahlung cross-section scales linearly with pressure (i.e., $\sigma_0 \propto p$). Consequently, plasma defocusing scales at a different rate,

$$\frac{L_{df}}{L_{pl}} \sim p^{m-2}. \tag{3.4}$$

Different plasma structures arising from changes in the pressure near the optimal regime of sequential filamentation are shown in Fig. 3.1. These simulations correspond to experimental parameters described in [52], where compression from 30 fs to 10 fs was demonstrated at an optimum pressure at 0.75 atm. The experimental input pulse with an energy of 0.7 mJ is collimated to a $1/e^2$ diameter of 0.5 cm and focused with a 100-cm lens, where the linear focus is approximately 40 cm within an argon gas cell. To find matching numerics, we use the following length scales: $L_{df}/L_{ds} = 4 \times 10^{-3}$, $L_{df}/L_{nl} = 1.3$, $L_{df}/L_{mp} = 3 \times 10^{-7}$, and $L_{df}/L_{pl} = 4 \times 10^{-6}$, which are consistent with the experimental parameters. Argon has an ionization energy of 15.7 eV, corresponding to $m = 11$, and at a pressure of 1 atm, $k_2 = 2.5 \times 10^{-8}$ fs^2 / nm and $n_2 = 1 \times 10^{-19}$ W / cm^2. The calculated Keldysh coefficient of $\beta^{(11)} = 10^{-140}$ cm^{19} / W^{10} yields an intensity $I_0 = 2 \times 10^{13}$ W/ cm^2, which leads to an LIB density of $N_0 = 7 \times 10^{10}$/cm^3. If we use an electron-neutral collision time at $p = 1$ atm of $\tau_c = 375$ fs, then $\sigma_0 \sim 5 \times 10^{-20}$ cm^2.

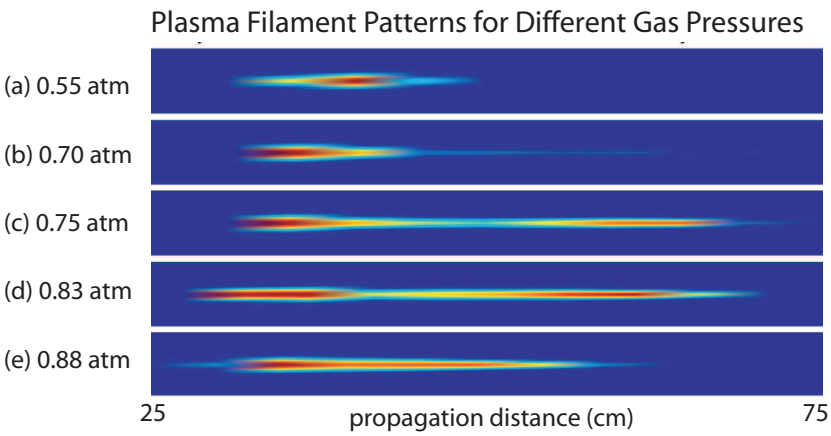

Figure 3.1: Predicted time-integrated and normalized plasma density as a function of propagation at different argon gas pressures: (a) 0.55 atm [$P = 0.95P_{cr}$] (b) 0.70 atm [$P = 1.2P_{cr}$] (c) 0.75 atm [$P = 1.3P_{cr}$] (d) 0.83 atm [$P = 1.35P_{cr}$] (e) 0.88 atm [$P = 1.42P_{cr}$]

Several trends in Fig. 3.1 are also evident in experiment and follow intuitively. At low pressures, we observe one plasma filament with a length approximately equal to one confocal parameter, as shown in Fig. 3.1(a). As we increase the pressure, the onset of filamentation occurs earlier due to increased contributions from self-focusing and plasma formation. At 0.7 atm, shown in the Fig. 3.1(b), we observe a light plasma trail after the first plasma filament, which increases in density as we increase pressure. When we tune to the optimum pressure at 0.75 atm, shown in Fig. 3.1(c), the double plasma structure is most distinct. Continuing to increase the pressure above this optimum results in the second filament both lengthening and drawing closer to the first, as shown in Fig. 3.1(d) at 0.83 atm. At 0.88 atm, the second structure nearly merges with first. In experiments [52], we observe off-axis multiple filamentation when the pressure exceeds approximately 1 atm.

Since the sequential filament pattern is not easily observed when the pressure decreases 10% below the optimum and since 10% above the optimal pres-

sure the sequential filaments have the appearance of one longer filament, one might expect that the double-plasma filament structure is difficult to access, yet we find that the dynamics are robust and observable over a range of beam and material parameters. As we increase the input pulse energy, the optimum double-filament structure occurs at slightly lower pressures, which increases the self-focusing to balance plasma effects. The greater contributions of self-focusing balance the higher pulse energies and yield more extended sequential plasma filament patterns.

Pulses at longer wavelengths and gases with higher ionization energies contribute to reduced ionization rates [59], which favors higher energy pulse compression. At longer wavelengths and lower input pulse powers, higher pressures are necessary to achieve the same ionization rates, in agreement with [52]. However, at higher pressures the dispersion-dominated post-shock dynamics [38] limit the length of plasma filaments, and a more tightly-focused geometry is necessary to observe sequential filamentation.

Plasma defocusing affects the development and evolution of a background field reservoir, and we propose that pulse compression via sequential filamentation scales to higher pulse energies at lower gas pressures, especially when plasma defocusing can be decreased accordingly. We recall that the relative contributions of plasma defocusing to multiphoton ionization scale inversely with τ_c^2, that is,

$$\frac{L_{df}}{L_{pl}} / \frac{L_{df}}{L_{mp}} \sim \tau_c^{-2}. \tag{3.5}$$

The electron collision time increases with lower gas pressure but also increases with atomic number [90, 68] due to Coulomb screening. We analyze how sequential filamentation could vary in different media in Fig. 3.2. The double-

structured on-axis peak-intensity curves coincide with two distinct plasma filaments with $P/P_{cr} = [0.95, 1.35, 1.8, 2.2]$, $L_{df}/L_{mp} = [3 \times 10^{-8}, 3 \times 10^{-7}, 3 \times 10^{-6}, 3 \times 10^{-5}]$ and $L_{df}/L_{pl} = [5.7 \times 10^{-8}, 1.2 \times 10^{-6}, 2.1 \times 10^{-5}, 2.7 \times 10^{-4}]$, respectively.

Longer plasma filaments with lower peak intensities are observed in materials with higher ionization rates and increased plasma defocusing, while shorter sequential plasma filaments occur at higher peak intensities with lower ionization rates and decreased plasma defocusing. To achieve similar dynamics at lower pressure, it is more favorable to use gases with smaller inverse bremsstrahlung cross-sections or higher atomic number to minimize the effects of plasma defocusing. Such materials also result in higher plasma densities in the sequential filament and may demonstrate additional plasma filament stages.

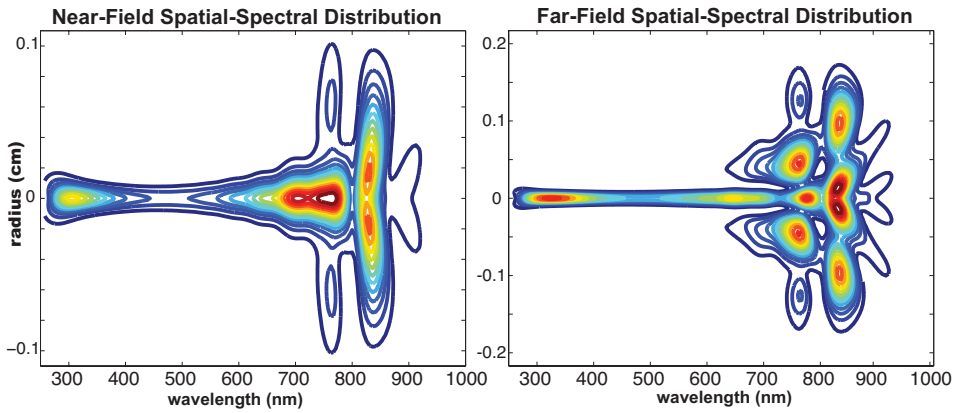

Figure 3.2: On-axis peak intensity as a function of propagation with different material parameters. Lines [blue, green, red, cyan] correspond to $P/P_{cr} = [0.95, 1.3, 1.8, 2.2]$, $L_{df}/L_{mp} = [3 \times 10^{-8}, 3 \times 10^{-7}, 3 \times 10^{-6}, 3 \times 10^{-5}]$ and $L_{df}/L_{pl} = [5.7 \times 10^{-8}, 1.2 \times 10^{-6}, 2.1 \times 10^{-5}, 2.7 \times 10^{-4}]$.

3.2 Nonlinear Dynamics of Sequential Filamentation

The sequential plasma filament structure we study here is formed by a two-peak temporal profile, where on-axis plasma defocusing of the front peak results in a background reservoir that feeds the rear peak [13, 63, 73]. To emphasize the spatial dynamics here, we show in Fig. 3.3(a) the contour plot of the fluence or time-integrated intensity as a function of propagation, which illustrates that each plasma filament has a distinctly different spatial beam profile. Figure 3.3(b) is the spatial beam profile at z = 40 cm, where the time-integrated spatial beam profile has a sink in the center due to multi-photon absorption. Approximately 5% of the initial pulse energy is lost to the production of plasma within the first filament structure. The resulting spatial beam profile with off-axis maxima requires higher powers for self-focusing [35], and with the combined effects of plasma defocusing, a substantial fraction of the pulse energy also diffracts after the first plasma filament.

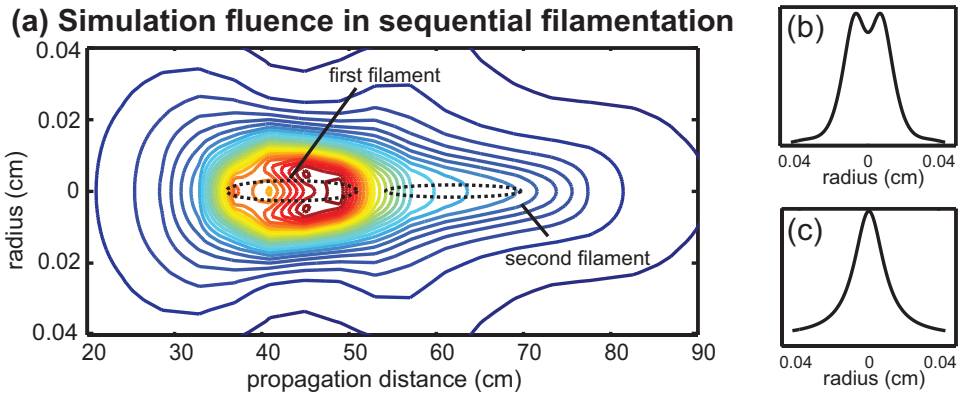

Figure 3.3: (a) Contour plot of fluence corresponding to Fig. 3.2 and $P = 1.3P_{cr}$. Contour lines are equally-spaced on a linear scale. The position of the plasma filaments are dotted. (b) Lineout of spatial beam profile at z = 40 cm. (c) Lineout of spatial beam profile at z = 70 cm.

As a consequence of plasma absorption and diffraction, lower peak-fluence

values are observed during the second filament, and in contrast to the first filament, the spatial beam profile during the second plasma filament has an *on*-axis maxima. In spite of lower fluence, ionization occurs due to the higher intensities resulting from self-compression [13, 41, 63] and increased shock-wave-induced self-focusing dynamics [38, 41]. At z = 70 cm, towards the end of the plasma filament, the spatial beam profile approaches a Townes profile [14, 77], as shown in Fig. 3.3(c), which has a narrower peak and wider wings than a Gaussian profile. This profile is the 2-D self-focusing attractor in the absence of plasma and is responsible for filamentation self-filtering of the spatial-mode [89].

When the ionization rate is low, the off-axis maximum in the spatial beam profile during the first plasma filament has a narrower radius, which suggests a higher power threshold for multiple filamentation. Since the self-focusing propagation dynamics are determined by the input spatial beam profile [28, 48], it is not surprising that shaping the input spatio-temporal profile and changing the relative contributions to the filament and background field reservoir in refocusing events can dramatically affect the propagation dynamics. It was recently demonstrated how the use of a circular mask on the input spatial beam profile improved the filamentation pointing stability and increased the spectral broadening [88]. Understanding the interplay between plasma defocusing and spatial replenishment in sequential filamentation may also explain pointing instabilities associated with polarization [101].

The significance of the sequential plasma filament in pulse compression can be observed in the spatial-spectral distribution, which indicates how the spectrum would change if apertured at the designated propagation distance. In Fig. 3.4 we plot the power spectrum as a function of radius at several distances of

propagation, corresponding to the optimally pressure-tuned scenario of sequential filamentation shown in Fig. 3.1(c). Before the first filament at z = 36 cm, depicted in Fig. 3.4(a), we observe that there has been slight broadening on-axis due to the higher intensities on-axis, but the broadening is generally symmetric and centered on-axis. At z = 43 cm, we see that the spectra has broadened most significantly off-axis [Fig 3.4(b)], due to the higher off-axis fluence as previously described in Fig. 3.3(b). At z = 51 cm [Fig. 3.4(c)], towards the end of the first plasma filament, the power spectra is centered on axis, and we see that the spectrum has broadened by approximately a factor of two. The spectra is slightly asymmetric with a sharper edge on the longer-wavelength edge. We note that after the first filament, the spectral broadening is not sufficient to explain the pulse compression observed at the output in experiments.

The sequential plasma filament is the signature of a dramatic spatial redistribution of spectral components. Between the end of the first plasma filament and the beginning of the second at z = 62 cm [Fig. 3.4(d)], we observe a highly asymmetric spectral distribution, where on-axis the power spectrum exhibits an extended blue-tail, which coincides with a red-wavelength-shifted background off axis. This trend continues towards the end of the second plasma filament, as shown in Fig. 3.4(e). At low pressures when there is only a single plasma filament [i.e., Fig 3.1(a)], no spatial-spectral reshaping occurs.

We confirm that spatial-spectral reshaping accompanies the propagation dynamics when the second filament merges with the first to produce the appearance of one longer filament, such as that observed at higher pressures shown in Fig. 3.1(e). In [93], the extensive blue-shifted spectrum is crucial to pulse self-compression, which suggests that the spatial-spectral redistribution we observe

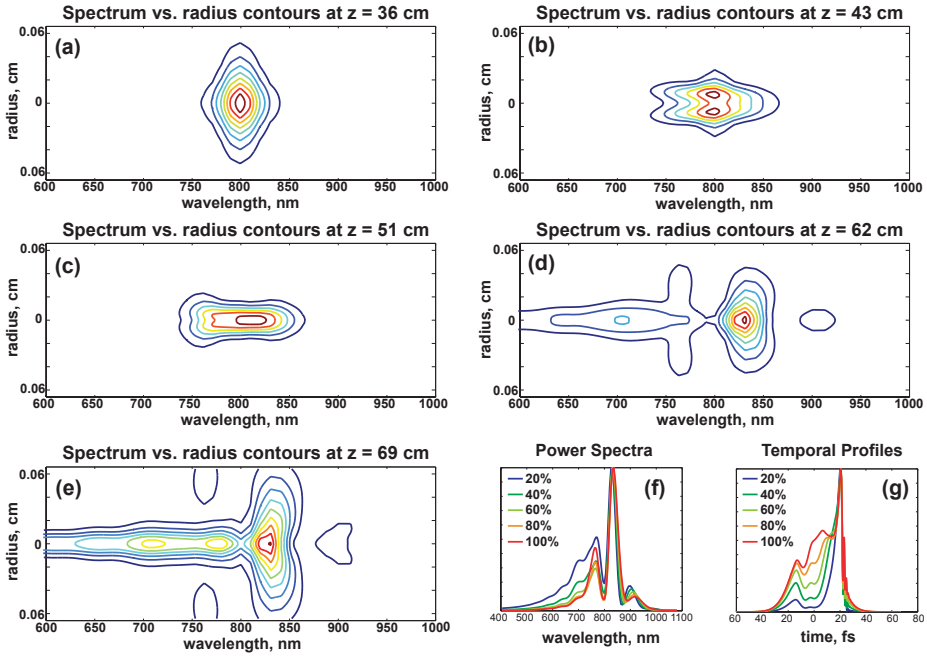

Figure 3.4: Contours of spectrum vs. radius at various distances during the optimized sequential filament propagation (a) at the onset of the first plasma filament stage at z = 36 cm, (b) in the middle of the first plasma filament at z = 43 cm, (c) near the end of the first filament at z = 51 cm, (d) at the onset of the second plasma filament stage at z = 62 cm, and (e) near the end of the second plasma filament. Aperture-dependent (f) power spectra and (g) temporal profiles at the sequential filament output z = 69 cm.

with sequential filamentation plays a general role in the pulse compression dynamics of filamentation. Similar observations of spatial-spectral reshaping in serial plasma filaments have been made [80] and were attributed to plasma-induced changes in the refractive index. We note that the electron density results in a lower refractive index and beam defocusing, which is incompatible with the explanation in [80].

Between the end of the first filament and the onset of the second, that is, between z = 51 and z = 63 cm, we observe comparable peak intensities, but

relatively lower fluence, and negligible contributions from plasma. Therefore, in contrast to previous assumptions, we cannot attribute the sudden extensive on-axis spectral broadening that occurs between the first and second filaments to self-phase modulation or plasma formation. Fluence and peak intensities are relatively low, and as we recall from Fig. 3.2, the sequential filament structure is observed even when initial peak powers are below the threshold for critical self-focusing. We extrapolate that the blue-compressible spectrum [93] is a combined effect of frequency-dependent space-time focusing and self-steepening. A comparison of the relative contributions in the nonlinear envelope equation [Eq. 1.71],

$$(\frac{L_{df}}{L_{nl}} T|u|^2 u)/(\nabla_\perp^2 T^{-1} u) \sim \omega^2, \tag{3.6}$$

which indicates that higher frequencies experience greater self-focusing. Equation 3.6 is not qualitative; it is a direct asymptotic limit for the coefficients as defined in Sec. 1.2. Consequently, it is the bluer frequencies that refocus after the first plasma filament to ionize and produce the second plasma stage. Although it is difficult to isolate the contribution of the sequential filament from that of the extended spatial confinement of light, our observations suggest that the two separated plasma channels not only coincide with the longest filament structures but result in minimal loss of pulse energy due to plasma formation and multiphoton ionization.

The resulting output beam is spatially inhomogeneous, as similarly described in [112], and in Fig. 3.4(f), we show the aperture-dependent power spectrum when 20%, 40%, 60%, 80%, and all of the power is transmitted. We observe the widest blue-shifted spectra on-axis, which also corresponds to the highest degree of compression. The total spatially-integrated power spectrum has only twice the initial input bandwidth, whereas on-axis, the spectrum has broadened

by almost a factor of four. We have approximately 30% power efficiency pulse compression to 10 fs, measured by the full-width half-maximum of the temporal profiles in Fig. 3.4(g). In the experiment, negatively-chirped output pulses are observed [51, 52, 93], which remains unexplained by the simulation model.

An illustration of spatial-spectral reshaping due to linear frequency-dependent propagation effects is shown in Fig. 3.5, where we provide contour plots of the spatial-spectral distribution for the two-filament structure corresponding to Fig. 3.4 at $z = 74$ cm [Fig. 3.5(a)] and the far-field spatial-spectral distribution found in the focal plane of an achromatic 100-cm lens, assuming aberration-free linear propagation after $z = 74$ cm [Fig. 3.5(b)] in which linear space-time focusing is included. Contours are equally-spaced on a linear scale. A comparison of the near and far-field plots both show similar blue-shifted spectra on-axis and red-shifted background, however the spatially-varying structures differ markedly due to linear space-time focusing effects. Spatial-spectral reshaping in the linear and nonlinear domains provides rigorous challenges for pulse characterization and measurement in both numerical and experimental investigations. In the far-field, we observe that the shortest pulse duration is no longer precisely on axis, and that the shortest self-compressed pulses are observed when integrating over a finite aperture size, which agrees with experiments.

In our simulations [Fig. 3.1] in which the pressure is varied, we observe that distinct sequential filamentatiion coincides with a maximal blue spectral tail, which we believe to be another indication of optimal spectral reshaping with serial filaments. This observation is in agreement with the experimental results provided in Ref. [88]. In Fig. 3.6 we plot the on-axis spectra with a

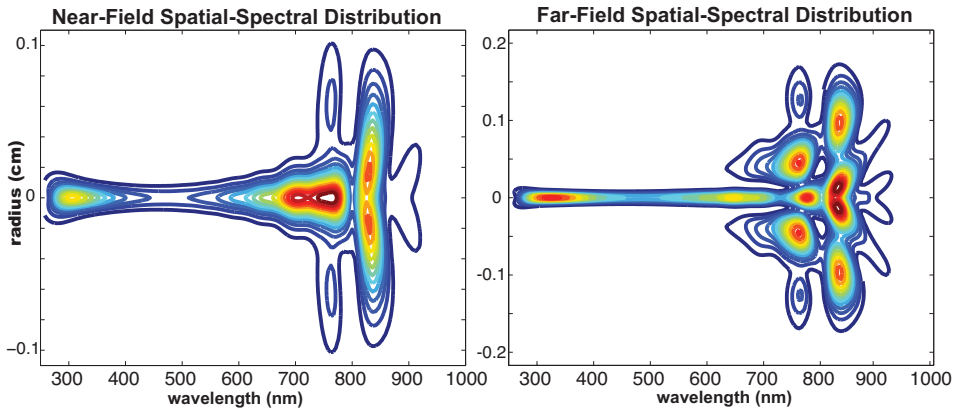

Figure 3.5: Spatial-spectral distributions after sequential filamentation with power $P = 1.3P_{cr}$ (a) at $z = 74$ cm and (b) in the far-field when imaged by a 100-cm lens, assuming linear propagation after $z = 74$ cm.

maximal norm of one, which corresponds to the pressure tuning in Fig. 3.1. The red curve, which corresponds to the maximal blue-tail, coincides with the most distinct sequential plasma filament pattern [Fig. 3.1(c)].

Longer sequential filamentation patterns have wider on-axis blue-shifted spectral tails, despite lower peak filament intensities [Fig. 3.2] and indicate that longer filament structures favor higher degrees of pulse compression. Our claim that higher-energy pulse compression via sequential filamentation occurs with shorter sequential filaments [Sect. 3.1] suggests that there exists a conjugate balance between pulse energy and pulse compression. In order to achieve both high energy pulses and a higher degree of pulse compression, precise control, tuning, and characterization of experimental parameters are required, which makes the spatial-spectral effects described in this paper highly relevant.

It is important to clarify that the spatial-spectral dynamics described here and associated with the sequential filament are entirely separate from conical emission. In fact, the radial dependence of frequencies in the output far-field

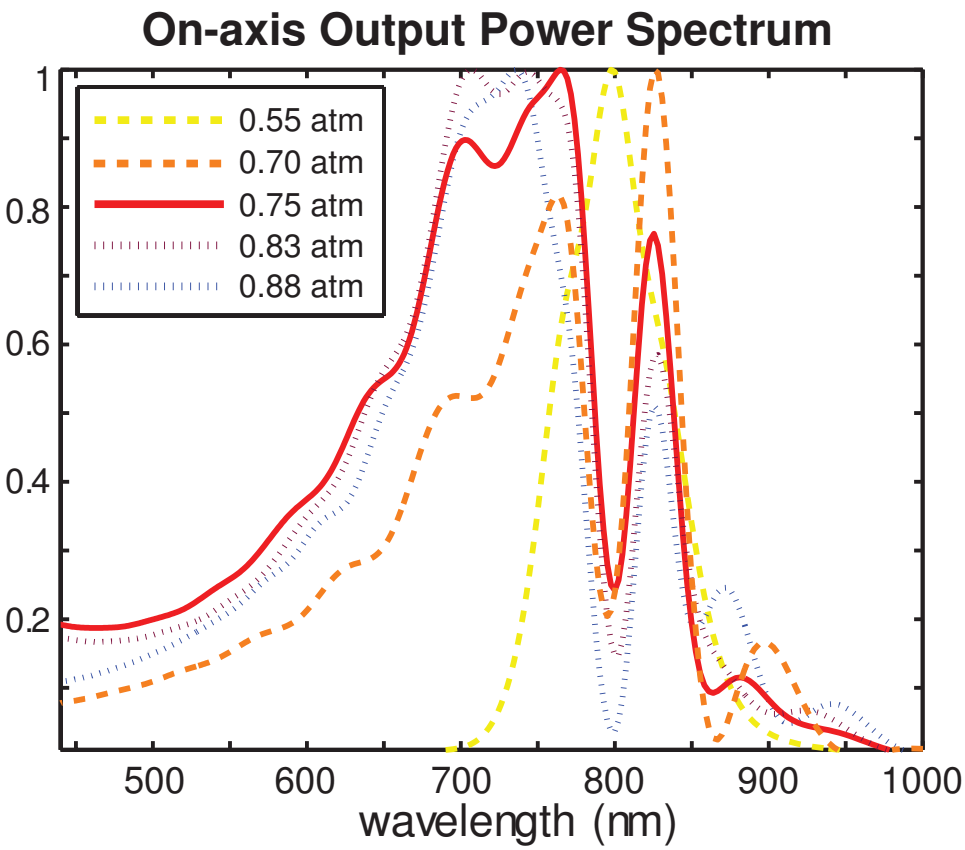

Figure 3.6: Output on-axis power spectra corresponding to Fig 1, for different pressures at the propagation distance at which the normalized plasma density has by approximately 2/3 of its value at the peak. The maximal blue-shoulder corresponds with the most distinct double-filament plasma structure in Fig. 1(c).

of normal-dispersion filamentation processes due to conical emission generally has a trend opposite to that of the processes described here and for larger bluer radii [12, 63, 80, 89], which is explained by phase-matched wave mixing [72]. Although dispersion is negligible in our configuration, subtle evidence of conical emission can be seen by comparing the change in lobe angle of the background spectra between Figs. 3.4(d) and 3.4(e). In Fig. 3.4(d) the off-axis spectral maxima align at 1-o'clock and 5-o'clock, and evolve in Fig. 3.4(e) to align more vertically. This angular shift indicates that the longer background wavelengths have

a smaller divergence. While conical emission is governed by the interplay of dispersion and self-phase modulation, the spatial redistribution of the spectral components emphasized in this article is most dramatic in the serial refocusing of the field background.

3.3 Discussion and Conclusion of Spectral Reshaping

Sequential filamentation underlines the fundamental propagation dynamics associated with more extended plasma filament production. The formation of a second plasma channel is the signature of maximal blue-shifted wavelengths in the background refocusing on-axis, extended spatial confinement of light with minimal pulse energy loss to multiphoton absorption and is the result of frequency-dependent space-time focusing and self-steepening effects. We show by simulation that two distinct sequential plasma filaments are the signature of optimal pulse compression [51, 52] and a maximally blue-shifted tail in the on-axis power spectrum [93]. Dramatic spatial-spectral reshaping occurs with the formation of the second filament in a process entirely separate from conical emission. We also describe the general dynamics that accompany the gas pressure tuning to optimize sequential filamentation and provide predictions for how pulse compression via filamentation can scale to higher powers. We anticipate that pulse compression efficiency and pointing stability can be improved with input spatial beam pulse shaping.

Future theoretical efforts aimed at integrating wavelength-dependent-dispersion curves and plasma-induced dispersion will improve our understanding of filamentation. The simulations are more challenging, however,

because the time and frequency-domain electric field envelopes are no longer fourier-transform pairs. In other words, if $\tilde{A}(r,\Omega,\zeta)$ is the pulse envelope in the frequency-domain, where $\Omega = \omega - \omega_0$, and $\widetilde{E}(r,t,\zeta)$ and $\tilde{E}(r,\omega,\zeta)$ are the electric fields in the time and frequency domains, then,

$$A(r,t,\zeta) = FT^{-1}\{\tilde{A}(r,\Omega,\zeta)\}e^{-i\omega_0 t}, \tag{3.7}$$

$$\tilde{E}(r,\omega,\zeta) = \tilde{A}(r,\omega-\omega_0,\zeta)e^{i(\tilde{k}(\omega))\zeta}, \tag{3.8}$$

$$\widetilde{E}(r,t,\zeta) = A(r,t,\zeta)e^{i\omega_0 t} \quad \otimes \quad FT^{-1}(e^{i(\tilde{k}(\omega))\zeta}), \tag{3.9}$$

where $\otimes$ is a convolution because the wavenumber $\tilde{k}(\omega)$ has time-dependence. Also, $\tilde{A}$ is the envelope of $\tilde{E}$ in the frequency domain, but A is not precisely the envelope of $\widetilde{E}$ in the time domain. Rederiving the nonlinear envelope equation in the frequency domain, we can calculate the frequency-domain evolution for the envelope, $\tilde{A}(r,\Omega,\zeta)$,

$$\tilde{A}_\zeta = \frac{-i}{2}\left[\tilde{\kappa}(\Omega)+k_1\Omega\right]^{-1}\left\{-\nabla_\perp^2\tilde{A}+\left[2\tilde{\kappa}(\Omega)+k_1\Omega\right]k_1\Omega\tilde{A}-\frac{4\pi}{c^2}\left[(\Omega+\omega_0)^2(\tilde{p}_n+i\tilde{p}_\alpha+i(\Omega+\omega_0)\tilde{j}\right]\right\}, \tag{3.10}$$

where $\kappa(\Omega) = k(\Omega+\omega_0)$. The nonlinear polarization that depends on changes in the refractive index is unchanged,

$$\tilde{p}_n(\Omega) = 3\widetilde{\chi}^{(3)}|A(\Omega)|^2A(\Omega), \tag{3.11}$$

but the absorptive part of the nonlinear polarization envelope $\tilde{p}_\alpha$ should computed differently than Eq. 1.60

$$\tilde{p}_\alpha = -\frac{m\hbar\omega_0}{(\Omega+\omega_0)^2}FT\left\{\frac{\partial^2\rho}{\partial\tau^2}FT^{-1}\left[(\tilde{A}^*)^{-1}e^{-i\kappa(\Omega)\zeta}\right]\right\}, \tag{3.12}$$

which requires either the additional storage or FT computations.

The current density should also be evaluated in the Fourier domain given by

Eq. 1.65,

$$j(\Omega) = \frac{e\rho\tau_c}{m}\frac{A(\Omega)}{1 - i(\Omega + \omega_0)\tau_c}. \tag{3.13}$$

This requires relatively little change in the current approach. However, for the calculation of the electron density, the multiphoton ionization rate should no longer be estimated by a constant over the bandwidth of the pulse and Eq. 1.50 becomes

$$\frac{\partial\rho}{\partial\tau} = FT^{-1}\left[\beta^{(m(\Omega))}(\Omega)\right]\frac{\left|FT^{-1}\left[\tilde{A}e^{i\kappa(\Omega)\zeta}\right]\right|^{m(\Omega)}}{m(\Omega)\hbar\omega_0}, \tag{3.14}$$

where, if we assume a linear approximation, then the Keldysh coefficient is:

$$\beta^{(m(\Omega))}(\Omega) \approx \beta^{(m)}(\Omega = 0) + b_1\Omega. \tag{3.15}$$

In principle, the inverse bremsstrahlung cross-section and electron collision time also have wavelength dependence, but these issues are a matter of definition.

The modeling for broadband pulses as described in this section would be essential for investigating higher harmonic generation and necessary for continuing research in pulse compression dynamics.

CHAPTER 4

CONCLUSION

In this thesis we have studied the nonlinear dynamics associated with the formation and propagation of light filaments in isotropic self-focusing media. In the first chapter, we investigated the collapse of optical vortices and demonstrated that the number of filaments resulting from azimuthal instabilities depends on the vortex beam power and topological charge. We showed that copropagating optical vortices with differing topological charge spatially-separate during filamentation and studied the associated nonlinear dynamics. The interaction coupled to the spatial separation between optical vortices results in power-dependent dynamics and changing torsional filament trajectories. In the second part of this thesis, we studied the spatiotemporal dynamics of sequential filamentation in noble gases, and showed that the alternating focusing and defocusing dynamics results in the spectral broadening that enables pulse compression. The author briefly discussed challenges associated with modeling broadband pulses, which would be important in future efforts studying high-harmonic generation and pulse compression via filamentation.

Additional directions for research involving the filamentation of optical vortices could develop the initial conclusions stated here of more complicated and even turbulent dynamics accompanying the self-focusing of inhomogeneously-polarized electric fields. As discussed in regards to the OAM Hall effect, the spatial separation of copropagating vortices leads to shifting gain curves associated with the growth of spatial instabilities and competing filamentation dynamics. Nonparaxial and higher-order vectorial corrections, particularly as they relate to angular momentum and inhomogeously-polarized fields, could be studied to

understand nonlinear dynamics beyond the 2-D Nonlinear Schrödinger Equation and these effects should also be observable in filamentation experiments. Although such higher-order corrections may not arrest collapse, they should influence the locations at which the filaments are formed. A simple experiment to demonstrate these effects would vary the temporal delay between orthogonal-circularly polarized vortices and investigate the transverse filamentation patterns. Since angular momentum exists due to the transverse spatial beam profile gradient, the growth of azimuthal instabilities accompanies a spatial redistribution of angular momentum, the understanding of which may be relevant to probing the motion nanoparticles in remote sensing applications.

Although investigations of polarization effects and angular momentum in propagating electromagnetic fields are currently limited to 2-D spatial dynamics, these effects may influence the temporal dynamics, particularly accompanying the formation of plasma. The author proposes that vectorial corrections to the nonlinear envelope equation should be investigated. At present, linear and circularly-polarized electric fields are typically modeled by rescaling propagation parameters, however, this approach provides only a qualitative comparison between linear and circular-polarization dynamics; vectorial or polarization effects associated with plasma formation dynamics are not integrated. Recent filamentation experiments investigating pulse compression [69], THz generation [20], and poynting stability [52], indicate that subtle differences in both spatial and temporal dynamics due to input beam polarization are not reconciled by the current analytical model. Since circularly-polarized electric fields impart torque to freely-moving charged particles, the plasma formed by circularly-polarized fields may generate a magnetic field.

The magnetic field produced by a circularly-polarized field would change direction depending on the circular polarization handedness. In underdense plasmas, theory suggests that circularly-polarized picosecond pulses with peak powers on the order of tens of terawatts produce relativistic electron velocities resulting in megagauss magnetic fields on-axis [49, 61]. Our initial calculations suggest that circularly-polarized femtosecond terawatt pulses produce plasma filaments in air with magnetic fields on-axis, which we should measure off-axis. Evidence of appreciable magnetic fields may indicate different mechanisms for energy absorption in plasma associated with different polarizations and may lead to new remote-sensing applications for filamentation.

BIBLIOGRAPHY

[1] C.N. Alexeyev and M.A. Yavorsky. Berry's phase for optical vortices in coiled optical fibres. *J. Opt. A*, 9:6, 2007.

[2] L. Allen, M.J. Padgett, and M. Babiker. The orbital angular momentum of light. *Prog. Opt.*, 39:291, 1999.

[3] S.M. Barnett. Angular momentum flux. *J. Opt. B*, 4, 2002.

[4] L. Bergé, C. Gouedard, J. Schjodt-Eriksen, and H. Ward. Filamentation patterns in kerr media vs. beam shape robustness, nonlinear saturation and polarization states. *Physica D*, 176:181, 2003.

[5] M.V. Berry. Quantal phase-factors accompanying adiabatic changes. *Proc. R. Soc. Lond. B*, 392:45, 1984.

[6] V. I. Bespalov and V.I. Talanov. Filamentary structure of of light beams in nonlinear liquids. *JETP Lett.*, 3:307, 1966.

[7] R.A. Beth. Mechanical detection and measurement of the angular momentum of light. *Phys. Rev.*, 50:115, 1936.

[8] M. S. Bigelow, N.N. Lepeshkin, and R.W. Boyd. Breakup of ring beams carrying orbital angular momentum in sodium vapor. *Phys. Rev. Lett.*, 92:083902, 2004.

[9] K.Y. Bliokh. Geometrical optics of beams with vortices: Berry phase and orbital angular momentum hall effect. *Phys. Rev. Lett.*, 97:043901, 2006.

[10] R.W. Boyd. *Nonlinear Optics*. Academic Press, 2003.

[11] A. Braun, G. Korn, X. Liu, D. Du, J. Squier, and G. Mourou. Self-channeling of high-peak power femtosecond laser-pulses in air. *Opt. Lett.*, 20:73, 1995.

[12] A. Brodeur, F.A. Ilkov, and S.L. Chin. Beam filamentation and the white light continuum divergence. *Opt. Commun.*, 129:193, 1996.

[13] S. Champeaux and L. Bergé. Femtosecond pulse compression in pressure-gas cells filled with argon. *Phys. Rev. E*, 68:066603, 2003.

[14] R. Y. Chiao, E. Garmire, and C.H. Townes. Self-trapping of optical beams. *Phys. Rev. Lett.*, 13:479, 1964.

[15] W.L. Collett, C.A. Ventrice, and S.M. Mahajan. Electromagnetic wave technique to determine radiation torque on micromachines driven by light. *App. Phys. Lett*, 82:2730, 2003.

[16] A. Couairon, M. Franco, A. Mysyrowicz, J. Biegert, and U. Keller. Pulse self-compression to the single-cycle limit by filamentation in a gas with a pressure gradient. *Opt. Lett.*, 30:2657, 2005.

[17] A. Couairon, S. Tzortzakis, L. Bergé, M. Franco, and A. Mysyrowicz. Infrared femtosecond light filaments in air: simulations and experiments. *J. Opt. Soc. Am. B*, 19:1117, 2003.

[18] F. Courvoisier, V. Boutou, J.Kasparian, E. Salmon, G. Mejean, J.Yu, and J.P. Wolf. Ultraintense light filaments transmitted through clouds. *Phys. Rev. Lett.*, 93:023901, 2004.

[19] M. C. Cross and P. C. Hohenberg. Pattern formation outside of equilibrium. *Rev. of Mod. Phys.*, 65:851, 1993.

[20] D'Amico, A. Houard, M. Franco, B. Prade, and A. Mysyrowicz. Coherent and incoherent radial thz radiation emission from femtosecond filaments in air. *Opt. Express*, 15:15274, 2007.

[21] R. Dasgupta and P.K. Gupta. Experimental observation of spin-independent transverse shift of the centre of gravity of a reflected laguerre-gaussian light beam. *Opt. Commun*, 257:91, 2006.

[22] A. Desyatnikov, C. Denz, and Y. Kivshar. Nonlinear optical beams carrying phase dislocations. *J. Opt. A*, 6:209, 2004.

[23] A. S. Desyatnikov, Y. Kivshar, and L. Torner. *Progr. Opt.*, 47:291, 2005.

[24] A.S. Desyatnikov, D. Mihalache, D. Mazilu, B.A. Malomed, and F. Lederer. Stable counter-rotating vortex pairs in saturable media. *Phys. Lett. A*, 364:231, 2007.

[25] A.S. Desyatnikov, D. Neshev, E.A. Ostrovskaya, Y.S. Kivshar, G. McCarthy, W. Krolikowski, and B. Luther-Davies. Multipole composite spatial solitons: theory and experiment. *J. Opt. Soc. Am. B*, 19:586, 2002.

[26] A.V. Dooghin, N.D. Kundikova, V.S. Liberman, and B.Y. Zeldovich. Optical magnus effect. *Phys. Rev. A*, 45:8402, 1992.

[27] A. Dubietis, E. Gaizauskas, G. Tamosauskas, and P. di Trapani. Light filaments without self-channeling. *Phys. Rev. Lett.*, 92:253903, 2004.

[28] A. Dubietis, G. Tamogauskas, G. Fibich, and B. Ilan. Multiple filamentation induced by input-beam ellipticity. *Opt. Lett.*, 29:1126, 2004.

[29] G. Duree, M. Morin, G. Salamo, M. Segev, B. Crosignani, P DiPorto, E. Sharp, and A. Yariv. Dark photorefractive spatial solitons and photorefractive vortex solitons. *Phys. Rev. Lett.*, 74:1978, 1995.

[30] S.R. Van Enk and G. Nienhuis. Photons in polychromatic rotating modes. *Phys. Rev. A*, 76:053825, 2007.

[31] M.D. Feit and J.A. Fleck Jr. Effect of refraction on spot-size dependence of laser-induced breakdown. *Appl. Phys. Lett.*, 24:169, 1974.

[32] Q. Feng, J.V. Moloney, A.C. Newell, E.M. Wright, K. Cook, P.K. Kennedy, D.X. Hammer, B.A. Rockwell, and C.R. Thompson. Theory and simulation on the threshold of water breakdown induced by focused ultrashort laser pulses. *J. Quantum. Electron.*, 33:127, 1997.

[33] A. Ferrando, M. Zacares, M.A. Garcia-March, J.A. Monsoriu, and P.F. de Cordoba. Vortex transmutation. *Phys. Rev. Lett.*, 95:123901, 2005.

[34] G. Fibich, S. Eisenmann, B. Ilan, and A. Zigler. Control of multiple filamentation in air. *Opt. Lett.*, 29:1772, 2004.

[35] G. Fibich and A. L. Gaeta. Critical power for self-focusing in bulk media and in hollow waveguides. *Opt. Lett.*, 25:335, 2000.

[36] G. Fibich, N. Gavish, and X.P. Wang. New singular solutions of the nonlinear schrödinger equation. *Physica D*, 211:193, 2005.

[37] G. Fibich and B. Ilan. Multiple-filamentation of circularly-polarized beams. *Phys. Rev. Lett.*, 89:013901, 2002.

[38] G. Fibich, W.Q. Ren, and X.P. Wang. Numerical simulations of self-focusing of ultrafast laser pulses. *Phys. Rev. E*, 67:056603, 2003.

[39] G. Fibich, Y. Sivan, Y. Ehrlich, E. Louzon, M. Fraenkel, S. Eisenmann, Y. Katzir, and A. Zigler. Control of the collapse in atmospheric propagation. *Opt. Express*, 14:4946, 2006.

[40] M. Fisher and C. Siders. *Proceedings of the Conference for Lasers and Electro-optics*, Long Beach, CA, 2005.

[41] A. L. Gaeta. Catastrophic collapse of ultrashort pulses. *Phys. Rev. Lett.*, 84:3582, 2000.

[42] A.L. Gaeta. Collapsing light really shines. *Science*, 301:54, 2003.

[43] E.J. Galvez, P.R. Crawford, H.I. Sztul, M.J. Pysher, P.J. Haglin, and R.E. Williams. Geometric phase associated with mode transformation of optical beams bearing orbital angular momentum. *Phys. Rev. Lett.*, 90:203901, 2003.

[44] M. Geissler, G. Tempea, A. Scrinzi, M. Schnurer, F. Krausz, and T. Brabec. Light propagation in field-ionizing media: extreme nonlinear optics. *Phys. Rev. Lett.*, 83:2930, 1999.

[45] I.S. Golubtsov, V.P. Kandidov, and O.G. Kosareva. Initial phase modulation of a high-power femtosecond laser pulse as a tool for controlling its filamentation and generation of a supercontinuum in air. *Quantum. Electron.*, 33:525, 2003.

[46] T. D. Grow and A. L. Gaeta. Dependence of multiple filamentation on beam ellipticity. *Opt. Express*, 13:4594, 2005.

[47] T.D. Grow, A.A. Ishaaya, L.T. Vuong, and A.L. Gaeta. Collapse and stability of necklace beams in kerr media. *Phys. Rev. Lett.*, 99:133902, 2007.

[48] T.D. Grow, A.A. Ishaaya, L.T. Vuong, A.L. Gaeta, N. Gavish, and G. Fibich. Collapse of super-gaussian beams. *Opt. Express*, 14:5468, 2006.

[49] M.G. Haines. Generation of an axial magnetic field from photon spin. *Phys. Rev. Lett.*, 87:135005, 2001.

[50] C.P. Hauri, W. Kornelis, F.W. Helbing, A. Heinrich, A. Couairon, A. Mysyrowicz, J. Biegert, and U. Keller. Generation of intense, carrier-envelope phase-locked few cycle laser pulses through filamentation. *Appl. Phys. B*, 79:673, 2004.

[51] C.P. Hauri, R.B. Lopez-Martens, C.I. Blaga, K.D. Schultz, J. Cryan, R. Chirla, P. Colosimo, G. Doumy, A.M. March, C. Roedig, E. Sistrunk, J. Tate, J. Wheeler, L.R. Di Mauro, and E.P. Power. Intense self-compressed, self-phase-stabilized few-cycle pulses at 2-μm from an optical filament. *Opt. Lett.*, 32:868, 2007.

[52] C.P. Hauri, T. Ruchon, F. Canova, E. Power, A. L'Huillier, and R. Lopez-Martens. Self-compression by ultrashort pulses in filaments. *presented at the Joint Symposium of the Conference for Lasers and Electrooptics and Quantum Electronics and Lasers Symposium*, Long Beach, California, 2006.

[53] G. Heck, J. Sloss, and R.J. Levis. Adaptive control of the spatial position of white light filaments in an aqueous solution. *Opt. Commun.*, 259:216, 2006.

[54] B.K.P. Horn and B.G. Schunck. Determining optical flow. *Artificial Intelligence*, 17:185, 1981.

[55] A.A. Ishaaya, L.T. Vuong, T.D. Grow, and A.L. Gaeta. Self-focusing dynamics of polarization vortices in kerr media. *Opt. Lett.*, 33:13, 2008.

[56] N. Ishii, L. Turi, V.S. Yakovlev, T. Fuji, F. Krausz, A. Baltuska, R. Butkus, G. Veitas, V. Smilgevicius, R. Danielius, and A. Piskarskas. Multimillijoule chirped parametric amplification of few-cycle pulses. *Opt. Lett.*, 30:567, 2005.

[57] J. Kasparian, M. Rodriguez, G. Mejean, J. Yu, E. Salmon, R. Bourayou H. Wille, S. Frey, Y.B. Andre, A. Mysyrowicz, R. Sauerbrey, J.P. Wolf, and L. Woste. White-light filaments for atmospheric analysis. *Science*, 301:61, 2003.

[58] J. Kasparian, M. Rodriguez, G. Mejean, J. Yu, E. Salmon, H. Wille, R. Bourayou, S. Frey, Y.B. Andre, A. Mysyrowicz, R. Sauerbrey, J.P. Wolf, and L. Woste. White-light filaments for atmospheric analysis. *Science*, 301:61, 2003.

[59] L.V. Keldysh. Ionization in the field of a strong electromagnetic wave. *Sov. Phys. JETP-USSR*, 20:1307, 1965.

[60] P. L. Kelley. Self-focusing of optical beams. *Phys. Rev. Lett.*, 15:1005, 1965.

[61] A. Kim. Axial magnetic fields in relativistic self-focusing channels. *Phys. Rev. Lett.*, 89:095003, 2002.

[62] M. Kolesik, E. M. Wright, A. Becker, and J. V. Moloney. Simulation of third-harmonic and supercontinuum generation for femtosecond pulses in air. *App. Phys. Lett.*, 88:153901, 2002.

[63] M. Kolesik, E.M. Wright, and J.V. Moloney. Dynamic nonlinear x waves for femtosecond pulse propagation in water. *Phys. Rev. Lett.*, 92:083902, 2004.

[64] S.O. Konorov, E.E. Serebryannikov, A.B. Fedotov, R.B. Miles, and A.M. Zheltikov. Phase-matched waveguide four-wave mixing scaled to higher peak powers with large-core-area hollow photonic-crystal fibers. *Phys. Rev. E*, 71:057603, 2005.

[65] V. I. Kruglov, Y.A. Logvin, and V.M. Volkov. The theory of spiral laser-beams in nonlinear media. *J. Mod. Opt.*, 39:2277, 1992.

[66] J. Leach, J. Courtial, K. Skeldon, S.M. Barnett, S. Franke-Arnold, and M.J. Padgett. Interferometric methods to measure orbital and spin, or the total angular momentum of a single photon. *Phys. Rev. Lett.*, 92:013601, 2004.

[67] V.S. Liberman and B.Y. Zeldovich. Spin-orbit interaction of a photon in an inhomogeneous medium. *Phys. Rev. A*, 45:8204, 1992.

[68] M.B.S. Lima, C.A.S. Lima, and L.C.M. Miranda. Screening effect on the plasma heating by inverse-bremsstrahlung. *Phys. Rev. A*, 19:1796, 1979.

[69] J. Liu, X.W. Chen, R.X. Li, and T. Kobayashi. Polarization-dependent pulse compression in an argon-filled cell through filamentation. *Las. Phys. Lett.*, 5:45, 2008.

[70] J.S. Liu, H. Schroeder, S.L. Chin, R.X. Li, and Z.Z. Li. Ultrafast control of multiple filamentation by ultrafast laser pulses. *App. Phys. Lett.*, 87:1611, 2005.

[71] M. Liu, N. Ji, Z. Lin, and S.T. Chui. Radiation torque on a birefringent sphere caused by an electromagnetic wave. *Phys. Rev. E*, 72:056610, 2005.

[72] G.G. Luther, A.C. Newell, J.V. Moloney, and E.M. Wright. Short-pulse

conical emission and spectral broadening in normally-dispersive media. *Opt. Lett.*, 19:789, 1994.

[73] M. Mlejnek, E.M. Wright, and J.V. Moloney. Dynamic spatial replenishment of femtosecond pulses propagating in air. *Opt. Lett.*, 23:382, 1998.

[74] M. Mlejnek, E.M. Wright, and J.V. Moloney. Femtosecond pulse propagation in argon: A pressure dependence study. *Phys. Rev. E*, 58:4903, 1998.

[75] K. D. Moll, D. Homoelle, A. L. Gaeta, and R. W. Boyd. Conical harmonic generation in isotropic materials. *Phys. Rev. Lett.*, 88:153901, 2002.

[76] K.D. Moll and A.L. Gaeta. Role of dispersion in multiple-collapse dynamics. *Opt. Lett.*, 29:995, 2004.

[77] K.D. Moll, A.L. Gaeta, and G. Fibich. Self-similar optical wave collapse: observation of the townes profile. *Phys. Rev. Lett.*, 90:203902, 2003.

[78] J. Moses and F.W. Wise. Soliton compression in quadratic media: high-energy few-cycle pulses with a frequency-doubling crystal. *Opt. Lett.*, 31:1881, 2006.

[79] D. Neshev, A. Nepomnyashchy, and Y.S. Kivshar. Nonolinear aharonov-bohm scattering by optical vortices. *Phys. Rev. Lett.*, 87:043901, 2001.

[80] E.T.J. Nibbering, P.F. Curley, G. Grillon, B. Prade, M.A. Franco, F. Salin, and A. Mysyrowicz. Conical emission from self-guided femtosecond pulses in air. *Opt. Lett.*, 21:62, 1996.

[81] M. Nurhuda, A. Suda, M. Hatayama, K. Nagasaka, and K. Midorikawa. Propagation dynamics of femtosecond laser pulses in argon. *Phys. Rev. A*, 66:023811, 2002.

[82] S. Oemrawsingh, J.A.W. van Houwelingen, E.R. Eliel, J.P. Woerdman, E.J.K. Verstegen, J.G. Kloosterboer, and G.W. 't Hooft. Production and characterization of spiral phase plates for optical wavelengths. *Appl. Opt.*, 43:688, 2004.

[83] K. O'Holleran, M.R. Dennis, F. Flossmann, and M.J. Padgett. Fractality of light's darkness. *Phys. Rev. Lett.*, 100:053902, 2008.

[84] A.T. O'Neill, I. MacVicar, L. Allen, and M.J. Padgett. Intrinsic and extrinsic nature of the orbital angular momentum of a light beam. *Phys. Rev. Lett.*, 88:053601, 2002.

[85] M. Onoda, S. Murakami, and N. Nagaosa. Hall effect of light. *Phys. Rev. Lett.*, 93:083901, 2004.

[86] S. Orlov and A. Stabinis.

[87] D.V. Petrov, L. Torner, J. Martorell, R. Vilaseca, J.P. Torres, and C. Cojocaru. Observation of azimuthal modulational instability and formation of patterns of optical solitons in a quadratical nonlinear crystal. *Opt. Lett.*, 23:1444, 1998.

[88] T. Pfeifer, L. Gallmann, M.J. Abel, D.M. Neumark, and S.R. Leone. Circular phase mask for control and stabilization of single optical filaments. *Opt. Lett.*, 31:2326, 2006.

[89] M. Franco Prade, A. Mysyrowicz, A. Couairon, H. Buersing, B. Eberle, M. Krenz, D. Seiffer, and O. Vasseur. Spatial mode cleaning by femtosecond filamentation in air. *Opt. Lett.*, 31:2601, 2006.

[90] J.F. Seely and E.G. Harris. Heating of a plasma by multi-photon inverse-bremsstrahlung. *Phys. Rev. A*, 7:1064, 1973.

[91] V.G. Shvedov, Ya. V. Izdebskaya, A.N. Alekseev, and A.V. Volyar. The formation of optical vortices in the course of light diffraction on a dielectric wedge. *Tech. Phys. Lett.*, 28:256, 2002.

[92] S. Skupin, L. Bergé, U. Peschel, F. Lederer, G. Mejean, J. Yu, J. Kasparian, E. Salmon, J.P. Wolf, M. Rodriguez, L. Woste, R. Bourayou, and R. Sauerbrey. Filamentation of femtosecond light pulses in air: turbulence versus long range clusters. *Phys. Rev. E*, 70:046602, 2004.

[93] S. Skupin, G. Stibenz, L. Bergé, F. Lederer, T. Sokollik, M. Schnurer, N. Zhavoronkov, and G. Steinmeyer. Self-compression by femtosecond pulse filamentation: Experiments versus numerical simulations. *Phys. Rev. E*, 74:056604, 2006.

[94] A.V. Sokolov, D.R. Walker, D.D. Yavuz, G.Y. Yin, and S.E. Harris. Femtosecond light source for phase-controlled multi-photon ionization. *Phys. Rev. Lett.*, 87:033402, 2001.

[95] M. S. Soskin and M. V. Vasnetsov. *Progr. Opt.*, 42:219, 2001.

[96] J. M. Soto-Crespo, E.M. Wright, and N.N. Akhmediev. Recurrence and azimuthal-symmetry breaking of a cylindrical gaussian-beam in a saturable self-focusing medium. *Phys. Rev. A*, 44:636, 1992.

[97] C.E.R. Souza, J.A.O. Huguenin, P. Milman, and A.Z. Khoury. Topological phase for spin-orbit transformations on a laser beam. *Phys. Rev. Lett.*, 99:160401, 2007.

[98] P. Sprangle, J.R. Penano, B. Hafizi, and C.A. Kapetanakos. Ultrashort laser pulses and electromagnetic pulse generation in air and on dielectric surfaces. *Phys. Rev. E*, 69:066415, 2004.

[99] G. Stibenz, N. Zhavoronkov, and G. Steinmeyer. Self-compression of millijoule pulses to 7.8 fs duration in a white-light filament. *ol*, 31:274, 2006.

[100] S.C. Tiwari. Geometric phase in optics and angular momentum of light. *J. Mod. Optics.*, 51:2297, 2004.

[101] A. Trisorio and C.P. Hauri. Control and characterization of multiple circularly-polarized filaments in argon gas. *Opt. Lett.*, 32:1650, 2007.

[102] S. Tzortzakis, B. Prade, M. Franco, and A. Mysyrowicz. Time-evolution of the plasma channel at the trail of a self-guided ir femtosecond laser pulse in air. *Opt. Commun.*, 181:123, 2000.

[103] A.J. Verhoef, J. Seres, K. Schmid, Y. Nomura, G. Tempea, L. Veisz, and F. Krausz. Compression of the pulses of a ti:sapphire to 5 femtoseconds at 0.2 terawatt level. *App. Phys. B*, 82:513, 2006.

[104] A. Vinçotte and L. Bergé. Femtosecond optical vortices in air. *Phys. Rev. Lett.*, 95:193901, 2005.

[105] L.T. Vuong and A.L. Gaeta. Orbital angular momentum hall effect via multiple-filamentation. *in progress.*, 2008.

[106] L.T. Vuong, T.D. Grow, A.A. Ishaaya, E.R. Eliel, G.W. 't Hooft, G. Fibich, and A.L. Gaeta. Collapse of optical vortices. *Phys. Rev. Lett.*, 96:133901, 2006.

[107] L.T. Vuong, A.A. Ishaaya, E.R.Eliel, and A.L. Gaeta. Curving light in isotropic nonlinear media. *in progress.*, 2008.

[108] L.T. Vuong, A.A. Ishaaya, T.D. Grow, A.L. Gaeta, and E.R. Eliel. Experiments showing orbital angular momentum exchange between vortex beams. *International Quantum Electronics Conference*, Munich, DE, 2007.

[109] N.L. Wagner, E.A. Gibson, T. Popmintchev, I.P. Christov, M.M. Murnane, and H.C. Kapteyn. Self-compression of ultrashort pulses through ionization-induced spatio-temporal reshaping. *Phys. Rev. Lett.*, 93:173902, 2004.

[110] G. Weisbuch, V. Buskens, and L.T. Vuong. Heterogeneity and increasing returns may drive socio-economic transitions. *Computational and Mathematical Organization Theory*, 2008.

[111] H.L. Xu, J. Bernhardt, P. Mathieu, G. Roy, and S.L. Chin. Understanding the advantage of remote femtosecond laser-induced breakdown spectroscopy of metallic targets. *J. Appl. Phys.*, 101:033124, 2007.

[112] A. Zair, A. Guandalini, F. Schapper, M. Holler, J. Biegert, L. Gallmann, U. Keller, A. Couairon, M. Franco, and A. Mysyrowicz. Spatio-temporal characterization of few-cycle pulses obtained by filamentation. *Opt. Express*, 15:5394, 2007.